



# Encapsulation of tin oxide layers on gold nanoparticles decorated one-dimensional CdS nanoarrays for pure Z-scheme photoanodes towards solar hydrogen evolution

Zhiyuan Peng, Yilu Su, Mohamed Sijaj<sup>\*</sup>

Department of Chemistry and Biochemistry, Université du Québec à Montréal, Montréal, QC, H3C 3P8 Canada

## ARTICLE INFO

### Keywords:

CdS/Au/SnO<sub>2</sub>  
Z-scheme photoanode  
Photoelectrochemical  
Hydrogen evolution  
1D hierarchical nanoarchitecture

## ABSTRACT

Despite their high potential for solar energy conversion into chemical fuels, most artificial all-solid-state Z-scheme photosystems have disordered structures and focus on power photocatalytic water splitting applications rather than photoelectrochemical (PEC) cells. Herein, an innovative pure Z-scheme heterostructure, CdS/Au/SnO<sub>2</sub>-S, composed of one-dimensional (1D) oriented CdS nanorods modified with SnO<sub>2</sub>-wrapped Au nanoparticles (NPs), was designed as a photoanode for highly efficient PEC hydrogen evolution. Systematic characterization confirms that the incorporated Au NPs not only act as the host platform to support the SnO<sub>2</sub> layer growth but also play a key role as the electron mediator for strengthening the vectorial charge transfer from SnO<sub>2</sub> to CdS. This reinforced Z-scheme charge transportation channel is favorable for suppressing the bulk charge recombination process, increasing the overall carrier density, and preserving the strong redox capability, ultimately resulting in a considerably improved photocurrent density and photo-to-current conversion efficiency with better corrosion resistance.

## 1. Introduction

The finite fossil fuels on Earth have been hard to burden with the growing requirements of continuous urbanization and industrialization, causing an increase in scientific interest in the search for alternative and renewable energy sources [1–4]. Hydrogen (H<sub>2</sub>), with its high energy capacity and clean attribute, is regarded as a promising and ideal candidate [5,6]. In the past decades, photoelectrochemical (PEC) water splitting based on photoactive materials has attracted considerable attention for directly converting the inexhaustible solar energy into hydrogen fuels in an economical and environmentally sustainable manner [7–9]. To accomplish reliable PEC devices with high photo-conversion efficiency, one major challenge is still the design and manufacture of semiconductor photoelectrodes with ideal light harvesting, superior photochemical stability, efficient charge carrier separation, and strong redox ability [10–12]. Although a variety of affordable photoactive materials have been developed, it is proven difficult for the single-component semiconductor to satisfy all the above physicochemical characteristics. In addition, their performances are greatly limited due to serious charge recombination in bulk, surface and interface, leading to a decline in the internal quantum efficiency [13].

Recent efforts have been devoted to the construction of semiconductor heterojunctions (usually Type-II heterostructure) to improve the carrier separation efficiency. However, the straddle charge transfer pathway will always weaken the redox ability of photo-generated electron-hole pairs, in which the charge carriers are driven into the conduction band (CB) and valence band (VB) of coupled semiconductors, respectively [14,15].

Comparatively, the artificial Z-schematic photosystem inspired by green plant photosynthesis is more desirable because it can not only improve the overall quantum efficiency but also retain the original strong redox capability by extinguishing electrons/holes with weaker redox potential [12,16]. In 2006, the concept of an all-solid-state Z-scheme photocatalytic system was proposed and rapidly developed [17], which usually comprises oxidation/reduction evolving semiconductors and the electron shuttle by using noble-metal particles (Au [12,18–20], Ag [21,22], Cd [23] and Pt [24]) and carbon-based additives like graphene oxide or reduced graphene oxide [14,25]. Nevertheless, until now most of the fabricated Z-scheme photosystems are disordered and focus on the power photocatalytic water splitting rather than PEC cells [26,27]. The direct contact of semiconductor components due to the inevitable aggregation of power samples will induce an

<sup>\*</sup> Corresponding author.

E-mail address: [sijaj.mohamed@uqam.ca](mailto:sijaj.mohamed@uqam.ca) (M. Sijaj).

<https://doi.org/10.1016/j.apcatb.2023.122614>

Received 21 November 2022; Received in revised form 1 March 2023; Accepted 8 March 2023

Available online 11 March 2023

0926-3373/© 2023 Elsevier B.V. All rights reserved.

undesirable back reaction, and puzzle the precise charge transport mechanism resulting from the coexistence of non-Z-scheme and Z-scheme models [14,28]. In fact, the critical factor in building an all-solid-state Z-scheme system is to realize the dynamic equilibrium of photoexcited charge carriers between two semiconductor components, which is believed not to be readily reached by a facile adjustment of semiconductor ratios if two semiconductor components are not totally detached by electron mediators [29]. Thus, to avoid the adverse non-Z-scheme charge transfer, various types of spatially separated Z-scheme PEC cells have been well designed for an unassisted overall water splitting [8,30–32], where two photoelectrodes (such as n-type photoanode and p-type photocathode) are in series and their majority carriers can recombine in the ohmic interfacial layer. Despite the efficient charge separation and preserved redox potentials, such a configuration, requiring light illumination and co-catalysts for both photoelectrodes, would greatly complicate the preparation process of PEC devices and curb its practical application. So, it is of great importance to come up with an all-solid-state Z-scheme photoelectrode in which the two semiconductor parts are completely separated by electron mediators for pure Z-scheme charge transfer while the carrier dynamic equilibrium can be easily reached by changing the ratios of the used semiconductors.

For an efficient PEC hydrogen evolution reaction, photoactive materials are essential, and their catalytic performance is strongly dependent on band structures. The cadmium sulfide (CdS) with a favorable bandgap value ( $\sim 2.4$  eV) and sufficient CB level for the reduction of  $H^+$  shows an excellent potential for solar conversion [33–36]. Hence, distinct CdS nanostructures with varied morphologies have been explored as photoanodes for PEC hydrogen evolution. In particular, one-dimensional oriented CdS architecture, like nanowire or nanorod, demonstrates relatively better PEC activity than other nanostructures, owing to its large length-to-diameter ratio and defined charge transport pathway with less electron loss [35,37–39]. However, as mentioned above, pure CdS photoelectrodes also suffer from excessive charge carrier recombination. In addition, the self-oxidation of  $S^{2-}$  caused by photoexcited holes prior to the surface oxidation reaction results in severe CdS photocorrosion and poor photostability [40,41]. Therefore, a large number of efforts have been focused on exploiting effective methods and strategies to push forward the advancement of CdS, mainly including co-catalyst loading [42], plasmon metal decorations [35,43], and heterojunction constructions (Type-II, Z-scheme and p-n junctions) [17,37,44]. Nevertheless, to the best of our knowledge, there have been no attempts and published reports regarding the fabrication of 1D CdS-based pure Z-scheme photoanodes toward excellent hydrogen evolution. Accordingly, in this work, we designed an innovative pure Z-scheme photoanode system, composed of a 1D hierarchical CdS/Au/SnO<sub>2</sub> nanorod array, for highly efficient PEC hydrogen production. The spectrum-defined hydrolysis-precipitation approach is first proposed and employed to selectively encapsulate the SnO<sub>2</sub> layer on Au NPs for achieving the spatial separation of CdS and SnO<sub>2</sub>. Here, the embedded Au NPs not only work as the host platform to support the attachment of the SnO<sub>2</sub> layer but also serve as the electron transfer mediators to profoundly promote the charge transfer from SnO<sub>2</sub> to CdS. This vectorial charge transportation helps to neutralize the VB holes of CdS and undermines the bulk recombination process of charge carriers, which is necessary for photoanode protection and the optimization of overall quantum efficiency. Meanwhile, the concentrated electrons in the CB of CdS with higher reductive power will drive faster hydrogen generation. As a result, the architected CdS/Au/SnO<sub>2</sub> photoanode exhibits significantly enhanced photo-to-current conversion efficiency, PEC property, and photostability compared to the pristine CdS.

## 2. Experimental section

### 2.1. Materials

The main chemicals involved in this work, including thiourea ( $NH_2CSNH_2$ , 99 %), glutathione ( $C_{10}H_{17}N_3O_6S$ , 98 %), cadmium nitrate tetrahydrate ( $Cd(NO_3)_2 \cdot 4 H_2O$ , 98 %), Gold (III) chloride solution ( $HAuCl_4$ , 30 wt%), Tin (II) chloride ( $SnCl_2$ , 98 %), methanol ( $CH_3OH$ ,  $\geq 99.8$  %) and ethanol ( $C_2H_5O$ , 95 %), were purchased from Sigma-Aldrich and utilized directly without further refinement. Fluorine-doped tin oxide glass substrates (FTO, 15  $\Omega$ /sq) and deionized water (18.2 M $\Omega$ -cm resistivity) were used throughout the whole experiment.

### 2.2. Fabrication of Au-coated CdS nanorod arrays

First, CdS nanorod arrays were prepared via a one-step hydrothermal process based on our previous studies [35]. Briefly, 0.5 mM of Cd ( $NO_3$ )<sub>2</sub>·4 H<sub>2</sub>O, 0.5 mM of thiourea, and 0.2 mM of glutathione were dissolved in 20 mL of deionized water and stirred until a clear solution was obtained, then transferred to a 25 mL Teflon-lined autoclave. Later, a fresh FTO substrate (2.5 × 1.0 cm) was cleaned with acetone, deionized water, and ethanol and placed in the autoclave wall, followed by the hydrothermal treatment at 200 °C for 4 h. Finally, the formed sample after washing and drying, was annealed at 400 °C for 1 h in nitrogen atmosphere for standby.

Subsequently, a facile in-situ reduction strategy was applied to evenly deposit Au nanoparticles on the surface of CdS nanorods. In detail, the prepared CdS nanorods on FTO substrates were immersed vertically into a mixture containing 10 mL of nanopure water and 10 mL of ethanol as the reducing agent. Then, different volumes (50, 100 and 200  $\mu$ L) of  $HAuCl_4$  solution (5 mM) were dropped into the reaction system. After holding for 2 h at room temperature, the Au-coated CdS nanorod arrays were washed slightly with deionized water and dried at 80 °C for about 12 h. Lastly, the formed electrodes were placed into a muffle furnace and subjected to a heat treatment at 400 °C for 1 h under N<sub>2</sub> flow at a heating rate of 20 °C min<sup>-1</sup>. The loading amount of Au nanoparticles was tuned by varying the  $HAuCl_4$  content in the precursor solution, and the corresponding samples were labeled as CdS/Au-0.5, 1, and 2, respectively.

### 2.3. Fabrication of selectively SnO<sub>2</sub>-encapsulated CdS/Au photoanodes

Selectively decorating a SnO<sub>2</sub> layer on obtained CdS/Au electrodes was achieved through a spectrum-defined hydrolysis-precipitation approach. Typically, FTO substrates with CdS/Au were soaked vertically into  $SnCl_2$  methanol solution (30 mL, 20 mM), followed by the addition of 50  $\mu$ L of NaOH solution (0.5 M) under gentle stirring. Later, the above photodeposition system was irradiated by a LED solar simulator (with a calibrated irradiation intensity of 100 mW/cm<sup>2</sup>) coupled with a 550 nm long-wave-pass filter. Upon photoreaction completion, the formed products were washed with ethanol, dried with N<sub>2</sub> flow, and then calcinated at 200 °C for 1 h in air for later characterizations. Here, photodeposition times (0.5, 1, and 2 h) were employed to adjust the loading thickness of the SnO<sub>2</sub> layer on the Au surface, and the final-obtained photoelectrodes were marked as CdS/Au/SnO<sub>2</sub>-S0.5, CdS/Au/SnO<sub>2</sub>-S1, and CdS/Au/SnO<sub>2</sub>-S2, respectively. For comparison, SnO<sub>2</sub>-coated CdS and fully SnO<sub>2</sub>-wrapped CdS/Au nanorod arrays were prepared by essentially identical procedures but with full-spectrum irradiation for 1 h, which were renamed as CdS/SnO<sub>2</sub> and CdS/Au/SnO<sub>2</sub>-F.

### 2.4. Analytical characterization

The exploration of crystallinity and structural features was taken on an X-ray diffractometer (Bruker D8 advance, Cu-K $\alpha$ ,  $\lambda = 1.5406$  Å). The surface chemical compositions of as-prepared photoanodes were precisely analyzed by X-ray photoelectron spectroscopy (XPS PHI 5600-ci,

Eden Prairie, MN, USA) with a monochromatized Al K $\alpha$  small-spot irradiation. Surface work functions of bare CdS nanorod arrays and SnO<sub>2</sub> thin film were determined by UV photoelectron spectroscopy using a He-I photon source (21.2 eV). The microstructure and surface morphologies were cautiously collected via a JSM7600F field emission scanning electron microscope (FESEM). Transmission electron microscopy (TEM) and high-resolution TEM investigations were conducted on a Jeol JEM-2100 F TEM instrument equipped with the energy dispersive X-ray detector (STEM-EDX). Photophysical information was obtained on a Lambda 750 UV-visible spectrometer. Inductively coupled plasma optical emission spectrometry (ICP-OES, Agilent Technologies, 5100) was employed to detect the relevant metal elemental contents in the as-prepared CdS/Au/SnO<sub>2</sub>-S photoanode. A PE LS-45 fluorescence spectrometer was applied to record the photoluminescence (PL) spectra at room temperature using a 375 nm excitation wavelength. Besides, the PL method was also selected to detect the hydroxyl radical ( $\cdot$ OH) formed during the photoreaction process, and terephthalic acid was used as the probe molecule. Specifically, powder photocatalysts scraped from FTO substrates were dispersed into a mixed aqueous solution (5 mL) of terephthalic acid (0.5 mM) and NaOH (2 mM) under vigorous stirring, which was then irradiated by simulated sunlight (AM 1.5 G) for 3 h. After the photoreaction, a 315 nm excitation wavelength was used to look at the solution with a QuantaMaster 40 spectrofluorometer.

## 2.5. PEC measurements

An electrochemical workstation (SP-200 Potentiostat) coupled with a conventional three-electrode quartz cell (as-fabricated samples as working electrodes, Ag/AgCl (3 M KCl) as the reference electrode, and a Pt wire as the counter electrode) was employed to collect photoelectrochemical information. The efficient coating areas on FTO substrates were controlled at around  $1.0 \times 1.0 \text{ cm}^2$ . A mixed NaSO<sub>3</sub> (0.35 M) and Na<sub>2</sub>S (0.25 M) aqueous solution (pH = 12.5) was applied as an electrolyte for all PEC and electrochemical experiments. An LSH-7320

ABA LED Solar Simulator with a calibrated irradiation intensity of  $100 \text{ mW/cm}^2$  was used as the light source to provide the natural spectrum. The polarization curves of as prepared photoanodes from  $-1.2 \text{ V}$  to  $0.4 \text{ V}$  (vs. Ag/AgCl) were recorded at a sweep rate of  $20 \text{ mV/s}$  under darkness, chopped illumination, or continuous sunlight illumination. The transient I-t measurements at a constant bias of  $0 \text{ V}$  vs. Ag/AgCl were executed under chopped sunlight illumination with eight on/off cycles (20 s). The incident photon-to-current efficiency (IPCE) measurements were carried out at an applied bias of  $0 \text{ V}$  vs. Ag/AgCl using an aligned monochromator with a wavelength range of  $320\text{--}700 \text{ nm}$ . Electrochemical impedance spectroscopy (PEIS,  $1\text{--}10^5 \text{ Hz}$ ) was performed at the open circuit potential with or without sunlight irradiation. Capacitance analysis over as prepared photoelectrodes was conducted at  $1 \text{ kHz}$  in darkness, ranging from  $-1 \text{ V}$  to  $0 \text{ V}$  vs. Ag/AgCl. The photostability of bare CdS and CdS/Au/SnO<sub>2</sub>-S photoanodes was tested at  $0 \text{ V}$  under AM 1.5 G irradiation. During the above process, the production of hydrogen in the gaseous phase of the sealed quartz PEC cell was collected and detected by a calibrated gas chromatograph (Perkin Elmer Clarus 580) and Ar was used as the carrier gas. Besides, some measured electrode potentials with respect to Ag/AgCl have been converted to those versus the reversible hydrogen electrode (RHE) through the Nernst equation for better comparison (Eq. S1).

## 3. Result and discussion

### 3.1. Structural analysis

The fabrication of Z-scheme hierarchical CdS/Au/SnO<sub>2</sub> heterojunction photoanodes is schematically depicted in Fig. 1a. Au NPs are firstly dispersed onto the surface of vertically aligned CdS nanorods with ethanol as the reducing agent. Following this, a facile photoassisted hydrolysis-precipitation approach is employed to selectively encapsulate the SnO<sub>2</sub> layer on Au NPs. In a typical process, surface plasmons of Au NPs can be photoexcited under visible light irradiation (with a

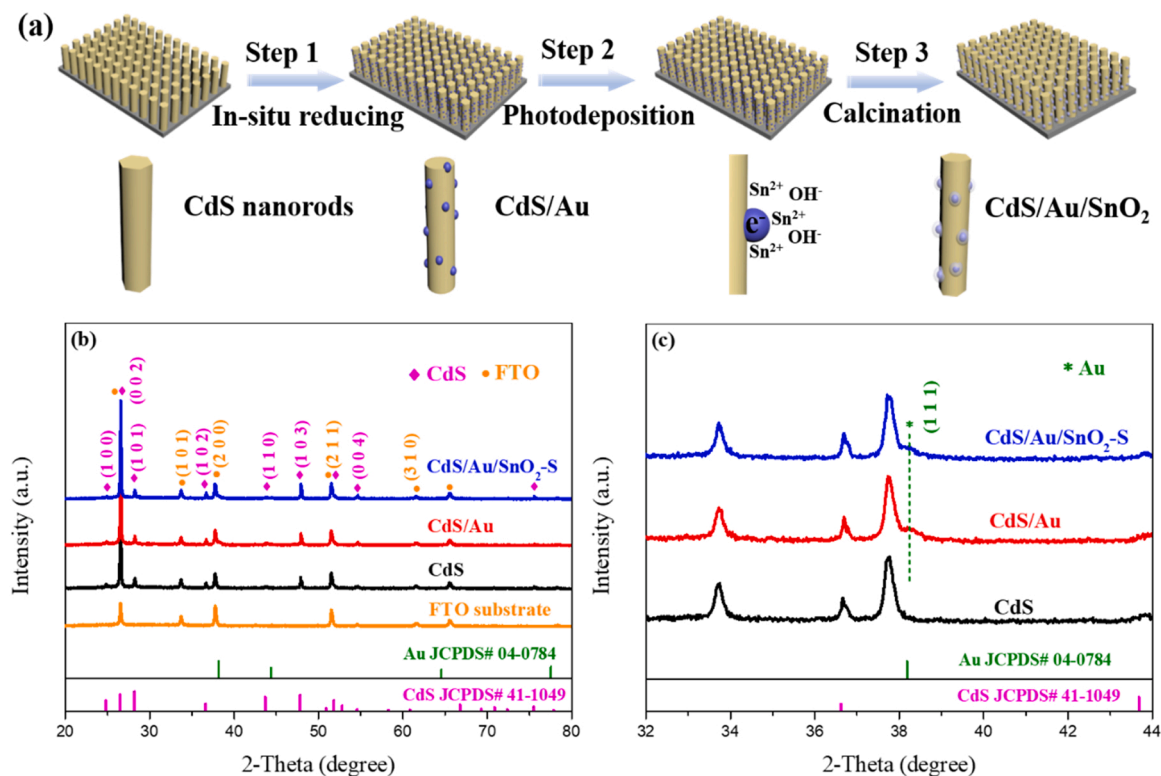


**Fig. 1.** (a) Schematic diagram for the synthetic route of 3D hierarchical CdS/Au/SnO<sub>2</sub> photoanodes. (b) X-ray diffraction patterns of as-fabricated CdS, CdS/Au, and CdS/Au/SnO<sub>2</sub>-S photoelectrodes. (c) Partial enlarged XRD patterns.

wavelength higher than 550 nm) and then decay to generate hot electrons above their Fermi level [45,46]. The electron-charged Au provides a large number of active sites for the approach and binding of  $\text{Sn}^{2+}$  via the electrostatic interaction [18]. Afterward, the attached  $\text{Sn}^{2+}$  on the Au surface would combine with  $\text{OH}^-$  due to the addition of NaOH and be thus hydrolyzed to be  $\text{Sn}(\text{OH})_2$ . Upon heat treatment in an air atmosphere, the intermediate hydroxide will be further dehydrated and oxidized to form  $\text{SnO}_2$ . Since the irradiated photon energy is insufficient for CdS photoexcitation, the controlled growth of the  $\text{SnO}_2$  layer will focus majorly on the Au surface, ultimately leading to the conformation of selectively  $\text{SnO}_2$ -encapsulated CdS/Au Z-scheme heterostructures. Similarly, one sun illumination will enable the fabrication of fully  $\text{SnO}_2$ -wrapped CdS/Au photoanodes, where photooxidation reaction will occur synchronously on the surface of CdS with better  $\text{SnO}_2$  deposition.

To investigate the composition and crystallographic features of as-fabricated CdS/Au/ $\text{SnO}_2$  Z-scheme heterojunctions, X-ray diffraction (XRD) analysis was performed and shown in Fig. 1b. Apart from characteristic peaks belonging to the FTO substrate, other diffraction peaks of the pristine CdS photoanode match well with those of hexagonal wurtzite CdS [37,47], corresponding to JCPDS Card No. 41-1049. A few auxiliary impurity peaks confirm its high quality. Meanwhile, the significantly enhanced characteristic peak around  $26.6^\circ$  mainly arises from the (002) crystal plane of CdS, indicating its preferential longitudinal growth along the [001] direction [48,49]. Notably, the introduction of the Au coating and the  $\text{SnO}_2$  layer displays a negligible influence on the CdS diffraction pattern. Fig. 1c shows the partially enlarged XRD patterns of bare CdS, CdS/Au, and CdS/Au/ $\text{SnO}_2$ -S photoelectrodes. One weak diffraction signal at  $2\theta$  values of  $38.2^\circ$  is detected and corresponds to the (111) diffraction of the cubic Au (JCPDS No. 04-0784) [50,51], implying the successful loading of metallic Au. Considering the diffraction interference of FTO substrates, the presence of  $\text{SnO}_2$  encapsulation will not be discussed here.

Comparative XPS studies were carried out to thoroughly probe the surface elemental compositions and chemical states of the hierarchical CdS/Au/ $\text{SnO}_2$  photoanode. The survey XPS spectrum of as-obtained

pure CdS and CdS/Au/ $\text{SnO}_2$  Z-scheme heterostructure is given in Fig. 2a. Except for the Cd and S signals, the appearance of intense Au and Sn peaks in the CdS/Au/ $\text{SnO}_2$  heterostructure is also distinctive compared with those of the CdS. High-resolution XPS spectra are displayed in Figs. 2b–2f. Two prominent peaks at binding energies of 405.5 and 412.4 eV correspond to Cd  $3d_{5/2}$  and Cd  $3d_{3/2}$  spin-orbits, demonstrating the cadmium oxidation state ( $\text{Cd}^{2+}$ ) in CdS [52,53]. The fitting results for S 2p spectrum (Fig. 2c) illustrate two characteristic peaks at 161.8 and 163 eV, consistent with the metal-sulfur bonds as the orbits of S  $2p_{3/2}$  and S  $2p_{1/2}$ . Noticeably, both Cd 3d and S 2p peaks of the CdS/Au/ $\text{SnO}_2$  heterostructure show a positive shift to higher binding energies, indicative of the decreased electron density on the CdS and the formation of strong interfacial interaction [54]. As for the Au region (Fig. 2d), binding energies appearing at 83.9 and 87.6 eV are designated to Au  $4f_{7/2}$  and Au  $4f_{5/2}$ , evidently manifesting the coating of Au NPs. More importantly, the Sn 3d spectrum (Fig. 2e) with two bands located at 487.3 and 495.7 eV is also detected in the hierarchical CdS/Au/ $\text{SnO}_2$  structure, which can be assigned to Sn  $3d_{5/2}$  and Sn  $3d_{3/2}$  spin-orbits. The splitting energy of 8.4 eV suggests the valence state of element tin ( $\text{Sn}^{4+}$ ) [13,55]. Correspondingly, the XPS signal of O 1s near 532.1 eV is attributed to crystal lattice oxygen in Sn-O. As a result, the above analysis provides convincing evidence for the successful fabrication of Au-coating and  $\text{SnO}_2$ -encapsulation in a CdS/Au/ $\text{SnO}_2$  heterostructure.

The typical SEM observations were developed to verify the morphologies of as-synthesized photoelectrodes. The low magnification SEM image in Fig. 3a reveals that the pristine CdS arrays featured as the 1D hexagonal rod-like shape almost vertically grow on the FTO substrate. From high magnification and cross-sectional SEM images (Figs. 3b and S1), it can be observed that the bare CdS nanorod possesses a relatively smooth surface with a diameter distribution from 100 to 300 nm, and the length scale is approximately 760 nm. After the in-situ reducing procedure, plenty of Au nanoparticles with an average size of 10 nm are well deposited on both the side and top surface of CdS nanorods (Fig. 3c). The as-fabricated CdS/Au/ $\text{SnO}_2$  heterostructure (Fig. 3d) exhibits an analogously morphological characteristic as that of CdS/Au nanorod arrays, but with slightly increased particle sizes,

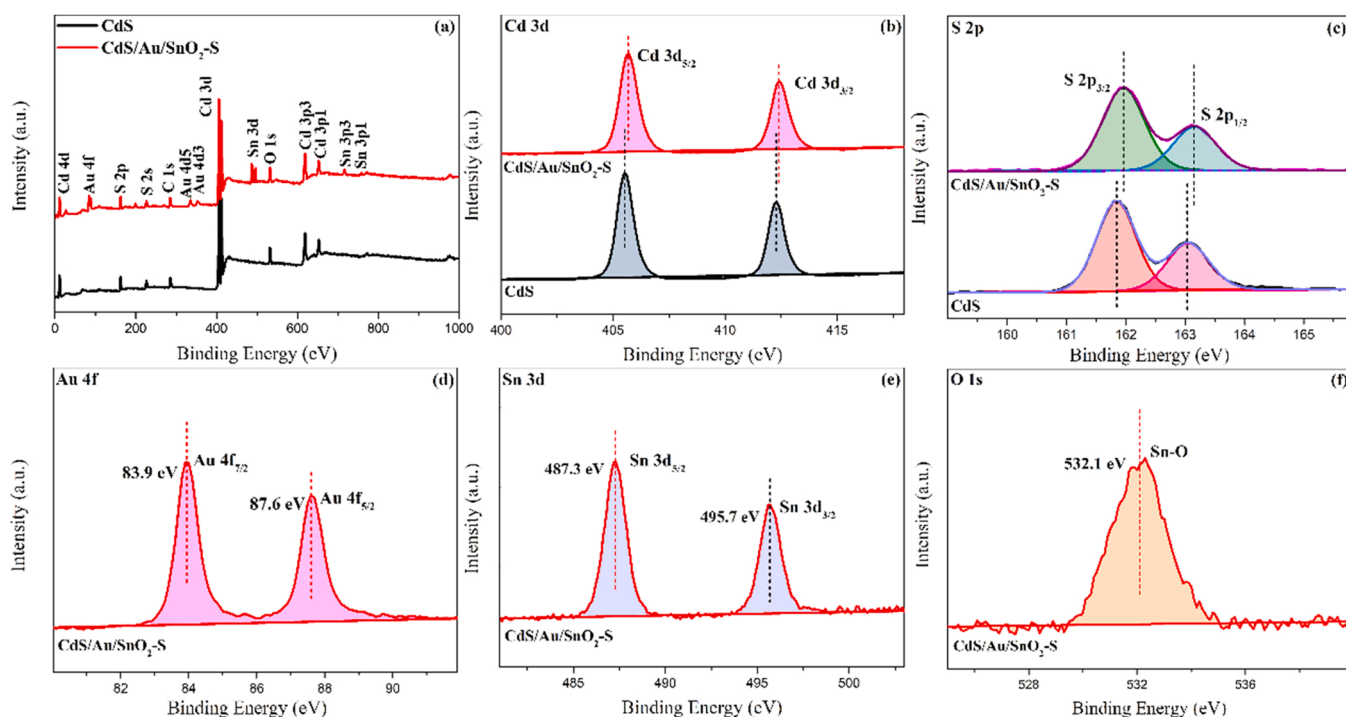


**Fig. 2.** (a) Comparative XPS survey scan of as-prepared CdS and CdS/Au/ $\text{SnO}_2$ -S photoanodes: (b–f) Relative high-resolution XPS spectra of Cd 3d, S 2p, Au 4f, Sn 3d, and O 1s regions.



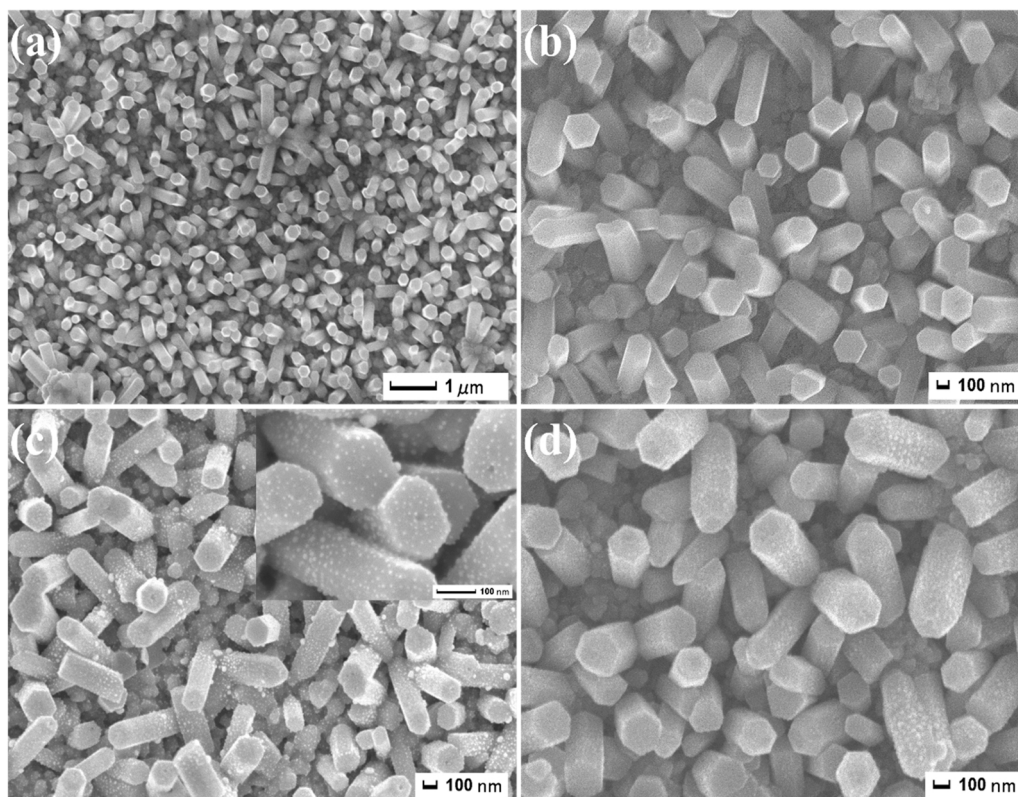


Fig. 3. Top-view SEM images of (a, b) the bare CdS, (c) CdS/Au, and (d) hierarchical CdS/Au/SnO<sub>2</sub> nanorod arrays.

demonstrating the favorable stability of the whole microstructure during the photoassisted hydrolysis-precipitation process.

TEM and HRTEM characterizations were applied to observe the detailed microstructures of CdS/Au/SnO<sub>2</sub>-S photoanodes and confirm the location of SnO<sub>2</sub> encapsulation. As shown in Fig. 4a, the CdS nanorod with the faceted and smooth surface has been successfully prepared through the hydrothermal process. The selected-area electron diffraction (SAED) pattern shown in the insert reveals its single-crystalline feature, which might endow it with high electron mobility for improving charge carrier transfer [49]. The detected 6.79, 3.58, and 3.16 Å spacings correspond to the (001), (100), and (101) crystal planes of hexagonal CdS, respectively. A clear interplanar distance of 0.67 nm shown in Fig. S2b is related to the {001} basal plane of CdS crystals, indicating its [001] growing direction. From the low magnification TEM image of CdS/Au nanorods (Fig. 4b), a large amount of consecutively distributed Au nanoparticles with well-proportioned particle sizes (in the range of 5–20 nm) can be readily distinguished on the pristine CdS nanorod surface, which is in a good agreement with the above SEM observations. The corresponding HRTEM image (Fig. 4c) presents the intimate interface connection between Au NPs and CdS nanorods with the exposed (111) crystal plane [56]. In addition, a SnO<sub>2</sub> wrapped CdS core-shell nanostructure was also fabricated via the photoassisted hydrolysis-precipitation process, but with full-spectrum illumination, and the related HRTEM image is displayed in Fig. S3. Obviously, the bare CdS nanorod is absolutely covered by a uniform SnO<sub>2</sub> sheath layer with a thickness of ~2 nm and a typical lattice distance of 0.335 nm can be assigned to its (110) crystal face. This compelling result proves that the photodeposition can indeed achieve the SnO<sub>2</sub> encapsulation on the photoactive material surface. Furthermore, Fig. 4d displays the low magnification TEM image of the CdS/Au/SnO<sub>2</sub> heterostructure. Upon the in-situ reducing and photodeposition process, the sample CdS/Au/SnO<sub>2</sub>-S still maintains the 1D rod-like microstructure without any deformation. Fig. 4e illustrates that the external SnO<sub>2</sub> passivation layer tightly attaches to the surface of Au NPs, signifying the successful

fabrication of hierarchical CdS/Au/SnO<sub>2</sub> heterojunction architecture. To further examine whether the deposition sites of SnO<sub>2</sub> are primarily on Au NPs, the TEM-EDX analysis with distinct regions taken from Fig. 4f (EDX1 concentrated on the bare CdS region and EDX2 focused on the CdS/Au/SnO<sub>2</sub> region) was performed, and the results are presented in Fig. S4. Apparently, area 1 is composed of Cd, S, Au, Sn, and O elements, but area 2 only contains Cd and S elements, which directly suggests the successful selective deposition of the SnO<sub>2</sub> layer on the Au surfaces of the CdS/Au nanorod. In general, the charge drift and diffusion behavior of a heterojunction are highly dependent on its structural features. Herein, such a special junction with uniform SnO<sub>2</sub> layers selectively covered on the Au surface of CdS/Au nanorods would be favorable for the realization of a Z-scheme charge transport mechanism, as discussed later. Ultimately, the energy dispersive X-ray spectroscopy (EDX) elemental mapping of Cd, S, Au, and O elements was recorded according to the HADDF-STEM image in Fig. 4g, and the correlative elemental distribution expresses a similar architecture as that of the CdS/Au/SnO<sub>2</sub>-S photoanode. Based on the above results, it is convinced that the strategy developed here can accomplish the selective encapsulation of the SnO<sub>2</sub> layer on Au NPs through varying the spectrum of irradiation.

### 3.2. Optoelectronic properties

The optical properties of as-obtained photoelectrodes were tested, and the resulted UV–vis absorption spectra are presented in Fig. S5. The pristine CdS nanorod arrays exhibit a remarkable visible-light harvesting capacity with a steep absorption onset of approximately 518 nm due to their intrinsic narrow bandgap [57,58]. Upon the decoration of Au NPs, an apparent absorption enhancement in the visible region accompanied with a slightly redshifted spectrum can be observed over the CdS/Au photoanode. The broad absorption band detected at 615 nm is mainly owing to the surface plasmon resonance effect of Au NPs [9]. After the SnO<sub>2</sub> encapsulation, CdS/SnO<sub>2</sub> and CdS/Au/SnO<sub>2</sub>-S photoelectrodes show similar absorption edges to bare CdS and CdS/Au

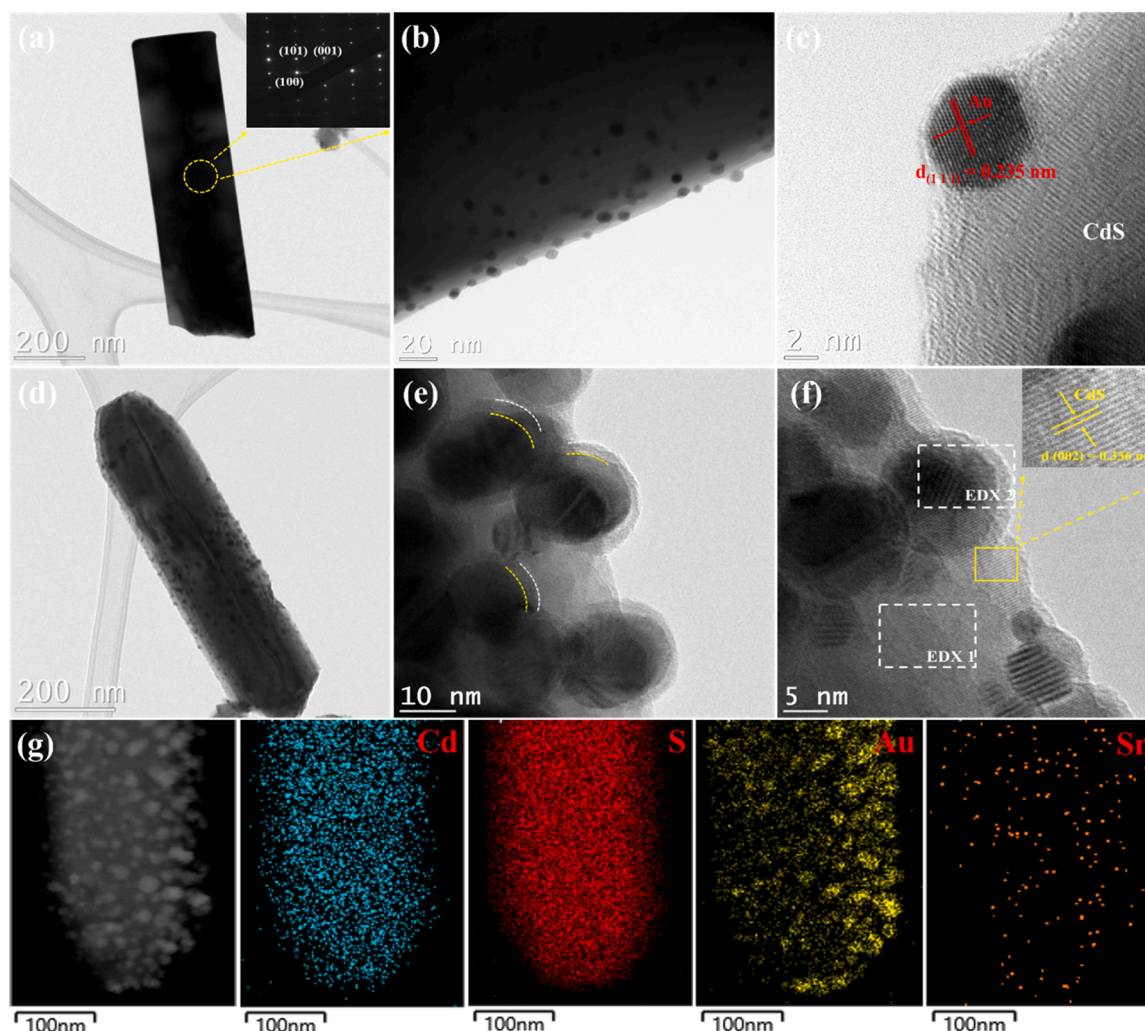


**Fig. 4.** (a) Low magnification TEM image and SAED pattern (insert) of the single-crystalline CdS nanorod. (b) Bright field and (b) HRTEM images of the Au-modified CdS nanorods. (d, e) Low magnification TEM and (f) HRTEM images of hierarchical CdS/Au/SnO<sub>2</sub> nanorods. (g) STEM image of CdS/Au/SnO<sub>2</sub> photoelectrode and the related EDX elemental mapping analysis.

nanorod arrays, but with the higher light sensitization below their absorption edge, which may be attributed to the higher absorption of scattered light by CdS [44]. It is believed that the prepared CdS/Au/SnO<sub>2</sub> photoanode with better light harvesting will obtain a higher quantum yield for PEC hydrogen evolution. In addition, the bandgap energies of as-fabricated photoelectrodes were estimated according to the Kubelka-Munk equation, and the calculated values (Fig. S5b) correspond to 2.29, 2.29, 2.25, and 2.25 eV, respectively.

For studying the PEC hydrogen evolution activities of as-fabricated photoelectrodes, the linear-sweep-voltammetry (LSV) curves were recorded using a conventional three-electrode configuration under one sun illumination. Initially, the impact of the loading amount of Au NPs on the photoelectrochemical performance of the pristine CdS nanorod arrays is systematically discussed (Fig. S6), and the optimal HAuCl<sub>4</sub> content is determined. Conceivably, excessive Au NPs coating would shield the light absorption of the CdS host and incur a profoundly inhibited photoresponse. Fig. 5a and S7 display the comparative polarization curves of the bare CdS, CdS/Au, CdS/SnO<sub>2</sub>, and CdS/Au/SnO<sub>2</sub>-S photoanodes with the photocurrent density as a function of voltage under dark, chopped, and continuous simulated sunlight irradiation. Apparently, the dark scans from  $-0.2$  V to  $1.1$  V vs. RHE only exhibit the ignorable current density, implying their high charge transport resistance. Under one sun illumination from the front side, the photocurrent density of all photoelectrodes promptly increases with the raised

applied bias. It is worth noting that the bare CdS nanorod array shows an unsatisfactory photoresponse with a considerably low photocurrent density ( $0.91$  mA/cm<sup>2</sup> at  $1$  V vs. RHE), due to its fast quantum recombination rate. After being coupled with an encapsulated SnO<sub>2</sub> layer, the resulting core-shell CdS/SnO<sub>2</sub> heterostructure possesses an evidently improved photocurrent density ( $3.06$  mA/cm<sup>2</sup> at  $1$  V vs. RHE) within the whole positive potential. Considering their matched energy band alignment and the higher conduction band (CB) potential of the CdS host (as demonstrated later) [13,37], a direct Z-scheme charge transfer route should be more suitable here than the conventional type-II heterojunction mode. Interestingly, the incorporation of Au NPs as the electron mediator can contribute to the higher PEC activity and result in a dramatically enhanced photocurrent density up to  $4.87$  mA/cm<sup>2</sup> (at  $1$  V vs. RHE), which may be attributed to the further promoted charge carrier separation efficiency. Besides, controlling samples with different photodeposition times for the SnO<sub>2</sub> encapsulation were fabricated and tested in Fig. S8 for the maximum PEC properties. From the ICP-OES analysis, the loaded Au and SnO<sub>2</sub> contents in the optimal CdS/Au/SnO<sub>2</sub>-S electrode were determined to be 2.75 and 7.49 wt%, respectively. Fig. 5b displays the difference in the photocurrent density between the front and back sides of the irradiation ( $100$  mW/cm<sup>2</sup>) for evaluating the separation and transfer processes of photoinduced holes. Obviously, the front-side photocurrent density of the bare CdS nanorod array was found to be 49 % higher than the back-side photocurrent density at an applied

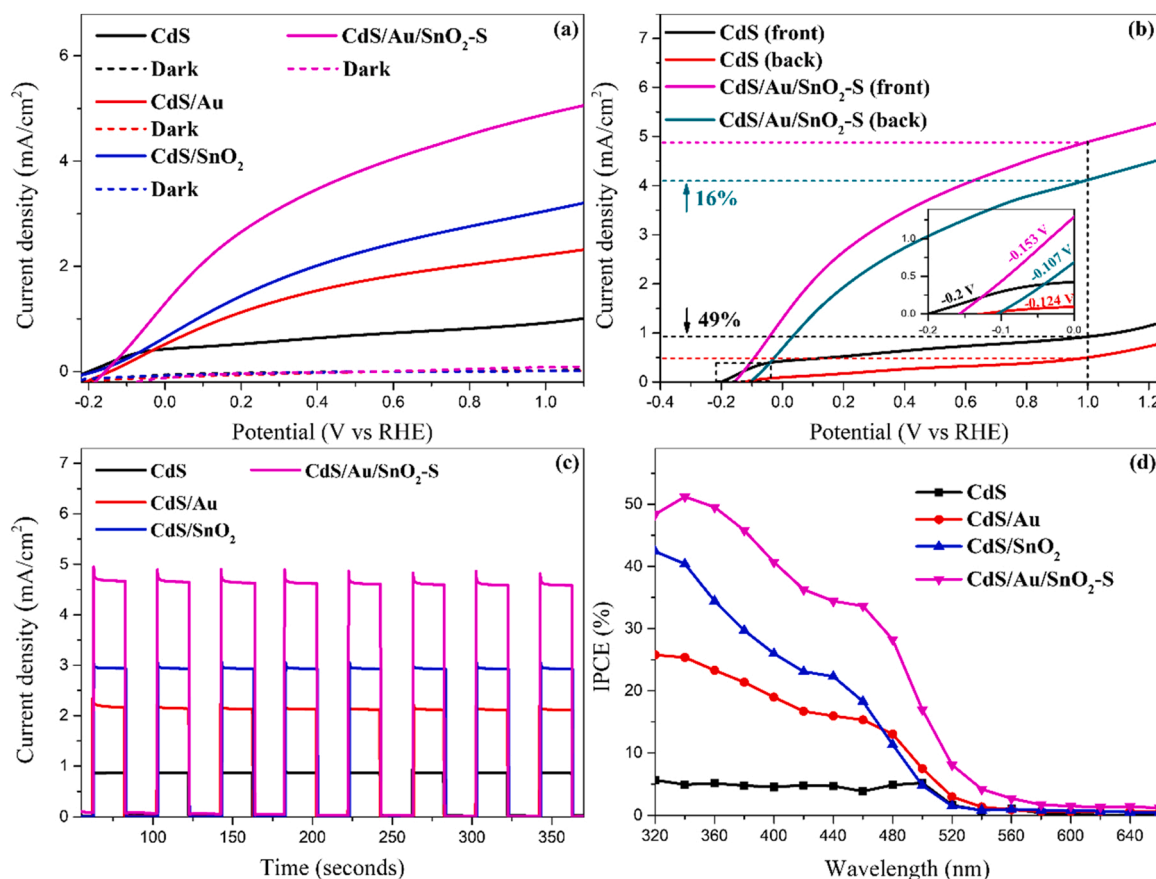


**Fig. 5.** Photoelectrochemical measurements on as-obtained CdS, CdS/Au, CdS/SnO<sub>2</sub>, and CdS/Au/SnO<sub>2</sub>-S photoanodes. (a) LSV curves under simulated sunlight irradiation (100 mW/cm<sup>2</sup>) and darkness. (b) The comparable current density-voltage curves under front or back side illumination. (c) Photoresponse tests at 0 V vs. Ag/AgCl under chopped light irradiation (8 cycles with 20 s of interval). (d) IPCE plots.

bias of 1 V vs. RHE, suggesting the high internal consumption of holes from the nanorod bottom (near the FTO substrates) [54,59]. This phenomenon means that holes are easily recombined with photogenerated electrons during the charge carrier transport process in the bulk semiconductor. By contrast, the largely reduced difference in photocurrent density (16 %) over CdS/Au/SnO<sub>2</sub>-S heterostructure reveals that the rational construction of the heterojunction can effectively suppress the charge carrier recombination behavior and allow more electrons to smoothly transfer into the counter electrode for hydrogen evolution. Such behavior is also certified by its less positive offset of onset potential (the insert).

Chronoamperometric I-t curves were obtained under AM 1.5 G irradiation (100 mW/cm<sup>2</sup>) without the applied bias for evaluating the instantaneous photoelectric behavior. As found in Fig. 5c, all fabricated photoelectrodes present a reliable and reproducible photocurrent response over repetitive on/off cycles of sunlight irradiation. Compared with the bare CdS nanorod array, both CdS/Au and CdS/SnO<sub>2</sub> yield a substantially higher photocurrent density, which might result from the passivation effect of Au NPs and the establishment of direct Z-scheme charge transport channels (as proved later). Notably, the 1D hierarchical CdS/Au/SnO<sub>2</sub>-S heterostructure demonstrates the maximum photocurrent generation for PEC hydrogen evolution, which is consistent with the above LSV analysis. Further, to investigate the correlation of photoactivity with respect to the incident wavelength, the IPCE tests (Eq. S2) were performed under monochromatic light illumination at 0 V vs. Ag/AgCl. As shown in Fig. 5d, the pristine CdS photoanode presents a relatively low photo-to-current conversion efficiency below 510 nm because of its rapid charge carrier recombination process. Upon the encapsulation of the SnO<sub>2</sub> layer with a high electron mobility [44], the

formed CdS/SnO<sub>2</sub> core-shell heterostructure exhibits a dramatically improved photoactivity from UV to visible light region, which may be ascribed to the enhanced optical absorption, facilitated charge separation and transport. After incorporating Au NPs as the electron mediator, its photoconversion efficiency is further improved and the corresponding IPCE plot presents a slight redshift, matching well with the result of UV-vis absorption analysis. Noticeably, the IPCE curve of the CdS/Au/SnO<sub>2</sub>-S photoanode increases sharply in the UV region and reaches a maximum at a wavelength of 340 nm, which may be closely associated with the activation of Z-scheme charge transfer channel. Ultimately, the well-designed CdS/Au/SnO<sub>2</sub>-S heterostructure demonstrates the optimal conversion efficiency (51.2 %) that is 10.4 times higher than that of the bare CdS photoanode. Based on these PEC performance measurements, it is believed that coupling the 1D CdS nanorod array with Au NPs and SnO<sub>2</sub> layer through an appropriate structured engineering strategy could accomplish the leap in photoelectrochemical activity. Moreover, through a comparison with reported similar CdS-based heterojunctions (Table S1), the novel 1D hierarchical CdS/Au/SnO<sub>2</sub>-S photoanode with the extremely excellent PEC activity demonstrates a certain superiority.

Long-term photostability and durability are crucial factors in evaluating the practical application of as-obtained PEC cells. Thus, the time-dependent photocurrents (Fig. 6a) over the pristine CdS and hierarchical CdS/Au/SnO<sub>2</sub>-S photoanodes were systematically examined under one sun irradiation without bias. As expected, the photocurrent density of the bare CdS decays rapidly with the prolonged irradiation time and the high attenuation ratio (16.8 % loss) in a period of 5000 s could be mainly owing to its highly susceptible photocorrosion. By sharp contrast, the hierarchical CdS/Au/SnO<sub>2</sub>-S heterostructure exhibits



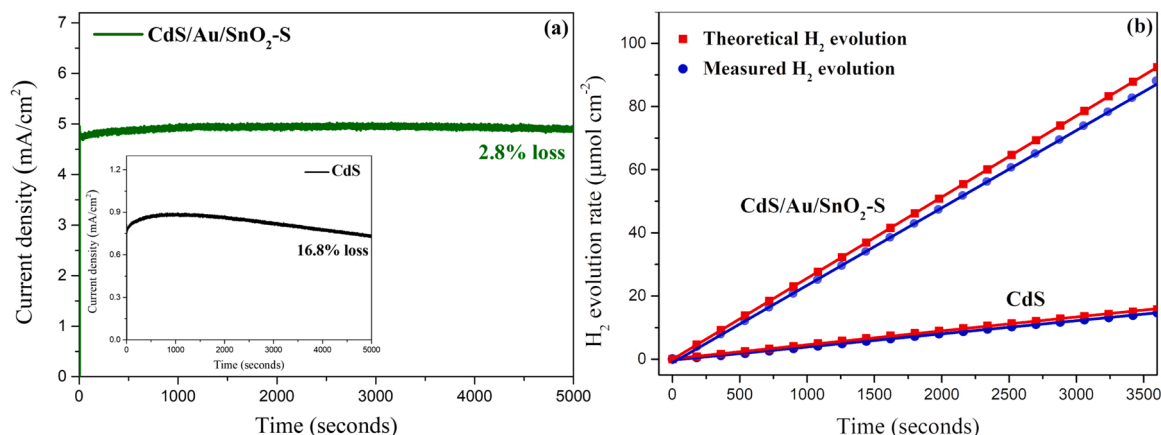


**Fig. 6.** (a) Long-term photostability and (b) time-dependent PEC hydrogen evolution over the pristine CdS and hierarchical CdS/Au/SnO<sub>2</sub>-S photoanodes under one sun irradiation (100 mW/cm<sup>2</sup>) at 0 V versus Ag/AgCl.

better stability (2.8 % loss) and the photocurrent density still retains at around 4.9 mA/cm<sup>2</sup> after 5000 s of continuous sunlight illumination, which possibly results from the efficient charge carrier separation and speedy extraction of VB holes in CdS. In addition, the cycled SEM image and XRD pattern (Fig. S9a and b) after the long-time photoreaction displays tiny micromorphological and crystal structural variations compared to the original sample, further confirming the wonderful photostability of the as-fabricated CdS/Au/SnO<sub>2</sub>-S photoelectrode. The above results experimentally reveal that the rational incorporation of Au NPs and SnO<sub>2</sub> layer can not only devote to the higher PEC performance but also protect the CdS host from photo-corrosion. In addition, the

generated hydrogen was collected and quantified every 3 min with a gas chromatograph, and the working areas of each photoelectrode were limited to 1 cm<sup>2</sup> with the identical experimental condition above. The detected H<sub>2</sub> amounts versus time is recorded in Fig. 6b. Both CdS and CdS/Au/SnO<sub>2</sub>-S photoanode present nearly linear increments in the yields of hydrogen. Relatively, the CdS/Au/SnO<sub>2</sub>-S heterojunction possesses a much higher average H<sub>2</sub> generation rate (1.47 μmol min<sup>-1</sup> cm<sup>-2</sup>) corresponding to its larger photocurrent density. Through comparing the measured H<sub>2</sub> amount with the theoretical H<sub>2</sub> production, the calculated Faradaic efficiency of CdS/Au/SnO<sub>2</sub>-S photoanode reaches up to 95.3 % (Eq. S4), signifying that the hydrogen evolution

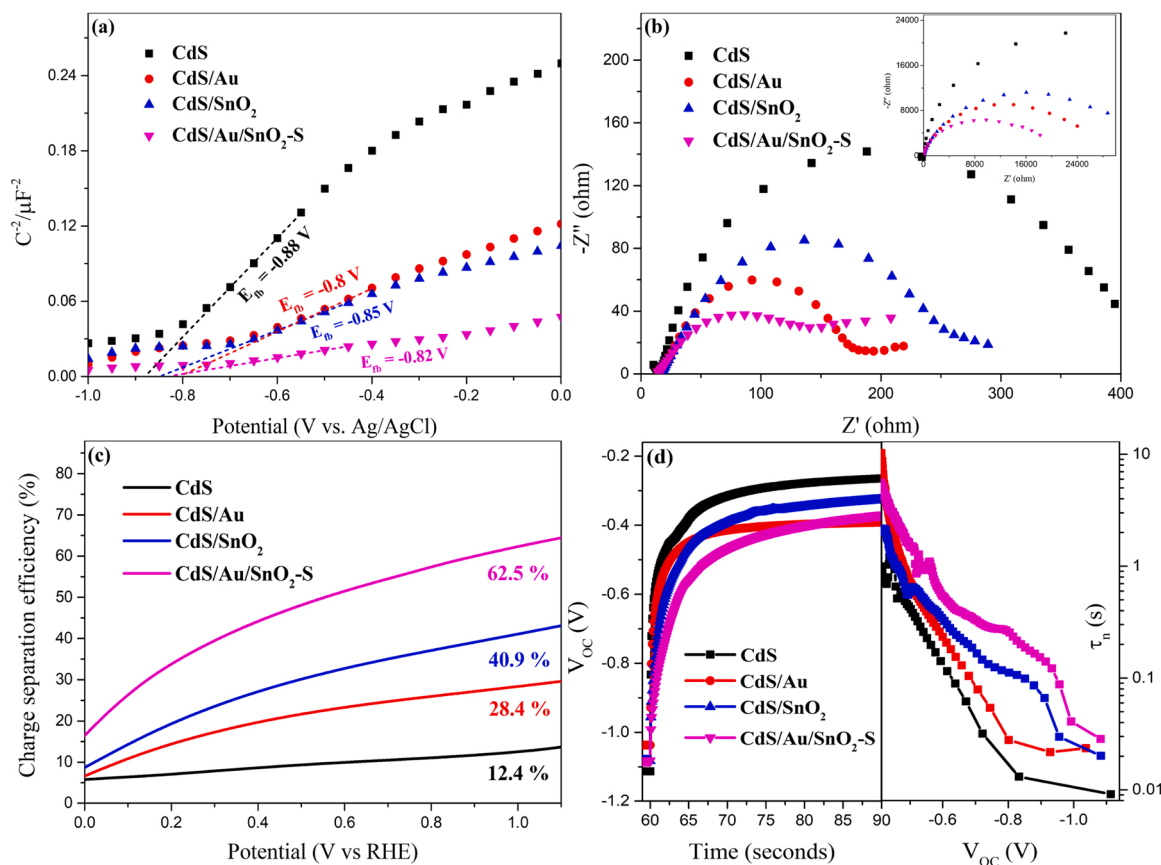


**Fig. 7.** (a) Mott-Schottky plots recorded at a frequency of 1 kHz, (b) Nyquist plots at the open circuit potential under darkness and one sun irradiation, (c) charge separation efficiency, (d) the open-circuit photovoltage decay curves (left), and calculated electron lifetimes (right) of as-prepared photoelectrodes.



reaction is responsible for the appearance of PEC photocurrent.

### 3.3. PEC enhancement analysis

To obtain a deep insight into the charge migration behavior responsible for the significant PEC enhancement, a series of electrochemical measurements were carried out. Mott-Schottky tests were first performed at a fixed frequency of 1 kHz with an applied bias from  $-1$  V to  $0$  V vs. AgCl under darkness. As shown in Fig. 7a, the M-S plots of all as-fabricated photoelectrodes present positive slopes, proving their n-type semiconductor characteristics. In the meantime, it is readily observable that the incorporation of Au NPs and SnO<sub>2</sub> layer leads to a progressively reduced slope, signifying the increased charge carrier density [60]. To be specific, the donor density ( $N_D$ ) of the pristine CdS, CdS/Au, CdS/SnO<sub>2</sub>, and CdS/Au/SnO<sub>2</sub>-S photoelectrodes were calculated to be  $4.04 \times 10^{17}$ ,  $9.5 \times 10^{17}$ ,  $1.12 \times 10^{18}$ , and  $2.85 \times 10^{18} \text{ cm}^{-3}$ , respectively (Eq. S5). The higher donor density of hierarchical CdS/Au/SnO<sub>2</sub>-S over 7 times higher than that of bare CdS further demonstrates the dramatically improved charge separation efficiency and better electrical conductance. It is speculated that this phenomenon is mainly caused by the formation of Z-scheme heterostructure (see below), so that the VB holes of CdS will be effectively captured by the CB electrons of the SnO<sub>2</sub> layer under the effect of the built-in electric field, thus leading to the suppressed electron-hole recombination process and higher  $N_D$  value. Besides, the passivation of Au NPs may also be favorable for the reduced surface state density along with less charge carrier recombination. Moreover, the flat-band voltage ( $E_{fb}$ ) was read through the x-intercept from the extrapolated linear part of  $C^{-2}$  vs the applied bias voltage. Compared with the bare CdS, a distinctive positive shift in the  $E_{fb}$  value of the CdS/Au/SnO<sub>2</sub>-S heterostructure means less electron-trapping process and higher quantum efficiency [60,61].

Electrochemical impedance spectra were recorded both under darkness and one sun irradiation to further analyze the charge transfer kinetics in the as prepared photoelectrodes. Figs. 7b and S10 present the obtained Nyquist plots and the associated equivalent circuit, which contains two resistances ( $R_s$  and  $R_{bulk}$ ): series resistance from the PEC cell and charge transfer resistance in the bulk component. Among them, CdS/Au and CdS/SnO<sub>2</sub> photoanodes exhibit a smaller semicircle radius in the high-frequency region, corresponding to a lower  $R_{bulk}$  than that of the pristine CdS, indicating the boosted charge carrier transport process [62]. As expected, upon the incorporation of Au NPs and a SnO<sub>2</sub> layer, the hierarchical CdS/Au/SnO<sub>2</sub>-S heterostructure with the smallest arc radius demonstrates the lowest resistance, thus allowing the more effective electron migration from SnO<sub>2</sub> to CdS. In addition, this result could also be confirmed by PL spectra, as shown in Fig. S11. The bare CdS nanorod array displays a strong visible band emission located at 515 nm and a relatively broad trap-state emission centered at around 680 nm [48,49]. In contrast to that of the CdS, the PL intensity of the as-fabricated CdS/Au/SnO<sub>2</sub>-S photoanode is sharply quenched on both band and surface trap state emission peaks, implying a largely suppressed bulk and trap-state-mediated carrier recombination process in the heterostructure because of the Z-scheme heterojunction fabrication and the passivation effect of Au NPs. Assuming the complete capture of photoinduced holes accumulated on the photoelectrode surface by the hole scavenger (Na<sub>2</sub>S/Na<sub>2</sub>SO<sub>3</sub>), the quantitative charge separation efficiency was calculated according to the following equation:  $\eta_{sep} = J_{ph}/J_{Max}$ , where  $J_{Max}$  (Eqs. S6 and S7) represents the maximum theoretical photocurrent density (Fig. S12). Following the UV-vis absorption spectra, the integrated photocurrent densities ( $J_{Max}$ ) of the pristine CdS, CdS/Au, CdS/SnO<sub>2</sub>, and CdS/Au/SnO<sub>2</sub>-S photoelectrodes are determined to be 7.44, 7.81, 7.38, and 7.87 mA/cm<sup>2</sup>, respectively. Fig. 7c displays the correlation for the calculated charge separation efficiency as a function of the applied bias voltage. Obviously, the architected CdS/Au/SnO<sub>2</sub>-S photoanode illustrates the highest separation efficiency in comparison to other photoelectrodes, up to 62.5 % at 1 V vs. RHE, directly verifying the promoted photoexciton

anti-recombination process in this heterostructure. It is noteworthy that the above analysis also reveals the important bridging role of embedded Au NPs on linking the SnO<sub>2</sub> layer to the CdS host for elevating the electron transport.

The instantaneous open-circuit voltage decay (OCVD) tests were applied to quantitatively evaluate the promoted charge separation efficiency and prolonged electron lifetimes. All photoelectrodes underwent a 30 s of sunlight illumination to gain a steady open-circuit voltage ( $V_{OC}$ ), and subsequently, the decayed  $V_{OC}$  curves as a function of time were examined in darkness, as displayed in Fig. S13 and the left image of Fig. 7d. The strongest  $V_{OC}$  decay observed in pristine CdS is majorly owing to the rapid bulk charge carrier recombination [56,63,64]. Comparatively, both Au decoration and SnO<sub>2</sub> wrapping result in effectively alleviated  $V_{OC}$  decay. With Au NPs, its surface passivation and formation of a Schottky rectifier in the plasmonic CdS/Au heterostructure will drive the delocalized holes to Au NPs for surface oxidation, thus preventing the charge carrier recombination, as proved previously [35,56]. With the SnO<sub>2</sub> layer, the conformation of the direct Z-scheme heterojunction (as analyzed later) will aid the rapidly vectorial charge migration from the SnO<sub>2</sub> layer to the CdS host, liberating the conduction band (CB) electrons of the CdS host and valance band (VB) holes of the SnO<sub>2</sub> layer for higher carrier density. It is worth noting that the utilization of embedded Au NPs in the middle of a core-shell CdS/SnO<sub>2</sub> nanostructure causes a very gentle  $V_{OC}$  decay, indicating further accelerated charge transfer and separation. The related decay lifetimes were calculated and shown in Fig. S13. Furthermore, the corresponding electron lifetimes ( $\tau_n$ ) were deduced in accordance with the  $V_{OC}$  decay rate (Eq. S8), and the results are shown in the right image of Fig. 7d. Obviously, the architected CdS/Au/SnO<sub>2</sub>-S heterostructure demonstrates a substantially prolonged lifetime compared to other photoelectrodes, which is well consistent with the above analysis. All previous results reasonably conclude that the rational incorporation of Au NPs and SnO<sub>2</sub> layer can advance charge separation and transfers, elongate electron lifetime, and benefit the outstanding PEC hydrogen evolution and photostability.

### 3.4. Au-mediated Z-scheme PEC mechanism

To elucidate the higher charge separation efficiency in hierarchical CdS/Au/SnO<sub>2</sub>-S heterostructure, the energetics of charge transport and a possible PEC catalytic mechanism were explored and proposed. In general, the charge carrier transfer behavior between semiconductors is determined by the interfacial energy-band bending, which is highly dependent on their Fermi levels and band structures [12,13,65–67]. Herein, the work function and valance band maximum (VBM) values of CdS and SnO<sub>2</sub> were characterized by ultraviolet photoelectron spectroscopy (UPS, Fig. S14a and b). Additionally, based on their optical bandgaps, the corresponding conduction band minimum (CBM) positions of CdS and SnO<sub>2</sub> were calculated to be  $-3.72$  and  $-4.26$  eV. As a result, a staggered band alignment among them is built as shown in Fig. S15, which matches well with previous reports [13,48]. As can be seen, the CdS host ( $-4.06$  eV) demonstrates a higher Fermi energy level than SnO<sub>2</sub> ( $-4.83$  eV). When they make direct contact, a charge migration process from CdS to SnO<sub>2</sub> will occur until a balanced energy level is reached, thus inducing the formation of an distinct built-in electric field. Meanwhile, the band edge of CdS will present an upward bending at the contact interface while a downward bending is presented on that of SnO<sub>2</sub>, ultimately disrupting the straddle charge transfer channels from CdS to SnO<sub>2</sub> (Type-II pathway), as shown in Fig. 8a and b. Subsequently, under sunlight irradiation, the presence of the built-in electric field will drive the photogenerated electrons in CB of SnO<sub>2</sub> to recombine with the holes in VB of CdS at the interface. The retained photoexcited charge carriers with higher redox potentials in CB of CdS and VB of SnO<sub>2</sub> will participate in the PEC system cycles, which illustrates a direct Z-scheme catalytic mechanism (Fig. 8c). Pioneering studies have pointed out that the introduction of the metallic polar

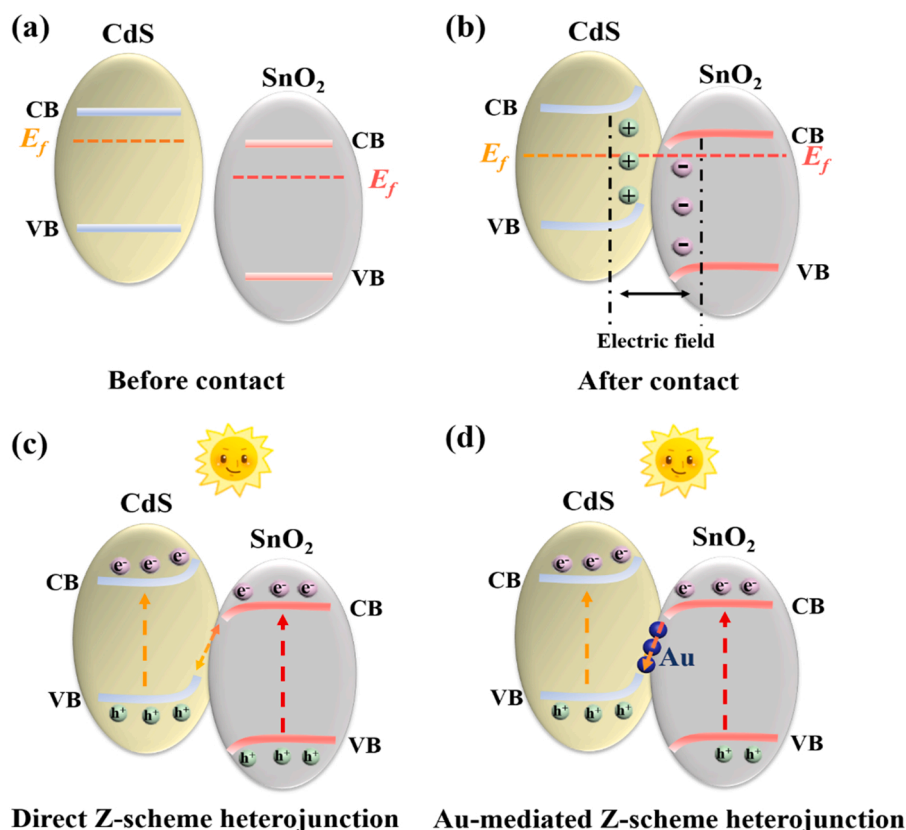


**Fig. 8.** Schematic illustrations of the band alignment of CdS and SnO<sub>2</sub> (a) before and (b) after contact. The charge transport behavior of (c) direct CdS/SnO<sub>2</sub> Z-scheme heterostructure and (d) Au-mediated CdS/SnO<sub>2</sub> Z-scheme heterojunction.

surface in direct binary Z-scheme photoactive systems through a rational structural engineering strategy will be favorable for a strengthened Z-scheme transport kinetic and improved PEC performance. Therefore, Au NPs with a higher work function ( $-5.30$  eV) are selected as electron mediators to accelerate the vectorial charge immigration from SnO<sub>2</sub> to CdS and perfect the Z-scheme transfer process (Fig. 8d), which has been confirmed by the further promoted charge separation efficiency in the CdS/Au/SnO<sub>2</sub>-S heterostructure compared to the binary CdS/SnO<sub>2</sub> (as analyzed above).

In order to further confirm the Z-scheme charge transfer route, the hydroxyl radicals ( $\cdot\text{OH}$ ) produced during the photoreaction were detected with terephthalic acid as the PL probe. As displayed in Fig. 9a, all fabricated photocatalysts present clear PL signals at around 425 nm, indicating the generation of hydroxyl radicals, which can be explained by comparing the energy band positions of CdS and SnO<sub>2</sub> with the redox potential of  $\text{OH}^-/\cdot\text{OH}$ . Fig. 9b exhibits the specific band alignment between CdS and SnO<sub>2</sub>, and the relative redox potential of  $\text{O}_2/\cdot\text{O}_2^-$  ( $-0.3$  V vs. NHE) and  $\text{OH}^-/\cdot\text{OH}$  ( $2.8$  V vs. NHE). Obviously, the photoexcited holes in the VB of SnO<sub>2</sub> with the higher oxidation potential can directly produce hydroxyl radicals, and photoinduced electrons in the CB of CdS are able to facilitate the generation of superoxide radicals ( $\cdot\text{O}_2^-$ ), indirectly producing hydroxyl radicals. Accordingly, if the charge transport route in the binary CdS/SnO<sub>2</sub> heterostructure majorly complies with the conventional Type-II pathway (Fig. S16), neither superoxide radicals nor hydroxyl radicals will be generated, which is contrary to the above PL results. Compared with that of the bare CdS, a stronger PL signal is clearly observed in the CdS/SnO<sub>2</sub>, revealing the more generation of hydroxyl radicals ( $\cdot\text{OH}$ ). This result evidently clarifies the efficient release of charge carriers with enough redox potentials in CB of CdS and VB of SnO<sub>2</sub>, suggesting the successful construction of the direct Z-scheme heterojunction. More importantly, the introduction of Au NPs as charge mediators could further promote the directional charge transfer

from SnO<sub>2</sub> to CdS, leading to higher quantum efficiency, which is verified by the highest PL intensity of the CdS/Au/SnO<sub>2</sub>-S heterostructure. When the discussion of energy bands and PL characterization are taken together, it seems likely that the charge-carrier immigration process in the CdS/Au/SnO<sub>2</sub>-S photoreaction system follows a Z-scheme catalytic model rather than the usual straddles band transfer.

Based on the aforesaid analysis, the rational charge carrier transport mechanism for the overall PEC hydrogen evolution over the hierarchical CdS/Au/SnO<sub>2</sub>-S heterostructure was proposed in Fig. 9c. Under one sun irradiation, electron-hole pairs can be first photo-generated on both CdS and SnO<sub>2</sub>. Owing to the more negative Fermi level of Au NPs, the photoexcited electrons in the CB of SnO<sub>2</sub> will rapidly travel into Au NPs. Meanwhile, since the VB potential of CdS is lower than the Fermi level of Au NPs, the gathered electrons in Au NPs will then directionally transfer to the CdS host, readily recombining with its VB holes. Thus, the photoinduced electrons and holes in the CdS host can be effectively separated through the collaboration with Au NPs and the SnO<sub>2</sub> layer, which is favorable for suppressing the charge carrier recombination process, reducing the bulk resistance, prolonging the electron lifetimes, and largely improving the photoelectric response. Note that Au NPs mainly function as the electron mediator to accelerate the vectorial charge immigration from SnO<sub>2</sub> to CdS. As a result, the effective release of electrons in CB of CdS with a stronger reduction ability will pass through the external circuit to the counter electrode for highly efficient hydrogen evolution, while the accumulated holes in VB of SnO<sub>2</sub> take part in the surface oxidation reaction. It should be mentioned that the promoted consumption of VB holes in the CdS host can also avoid its  $\text{S}^{2-}$  self-oxidation for better photoanode protection and long-term stability.

Herein, we would like to emphasize that the configuration variance plays an unignorable role in interfacial charge transport and PEC performance enhancement of the all-solid-state Z-scheme CdS/Au/SnO<sub>2</sub> photoanode. To confirm the structural superiority of the hierarchical

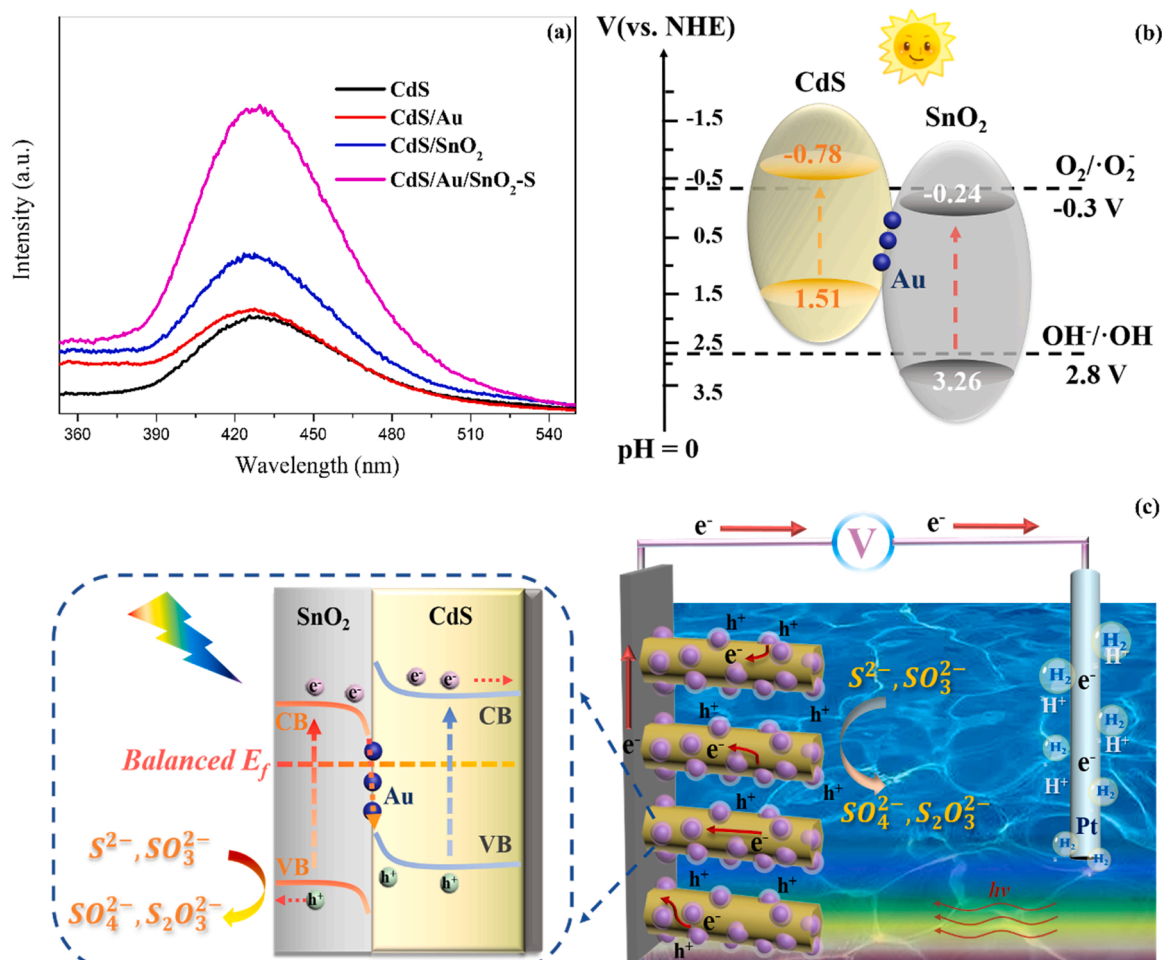


**Fig. 9.** (a) Comparative PL spectra for the detection of hydroxyl radicals ( $\cdot\text{OH}$ ) over the CdS, CdS/Au, CdS/SnO<sub>2</sub>, and CdS/Au/SnO<sub>2</sub>-S photocatalysts. (b) Band alignment between CdS and SnO<sub>2</sub>, and the relative redox potential of O<sub>2</sub>/·O<sub>2</sub><sup>-</sup> and OH·/·OH. (c) Schematic diagram of charge transfer mechanism for the overall PEC hydrogen evolution over the CdS/Au/SnO<sub>2</sub>-S photoanode.

CdS/Au/SnO<sub>2</sub>-S photoanode, full-spectrum illumination was used to fabricate the complete SnO<sub>2</sub>-wrapped 1D CdS/Au nanorod array (CdS/Au/SnO<sub>2</sub>-F) for comparison. As displayed in the TEM observations of the CdS/Au/SnO<sub>2</sub>-F sample (Fig. S17), the SnO<sub>2</sub> passivated layer is not only photo-deposited on the Au surface but also attached to CdS nanorods, verifying the formation of the complete encapsulation configuration. Meanwhile, the comparative LSV curves and PL detection (Fig. S18a and b) reveal that the fully encapsulated CdS/Au/SnO<sub>2</sub>-F photoanode exhibits a relatively lower photocurrent density (3.86 vs. 4.87 mA/cm<sup>2</sup> at 1 V vs. RHE) and less generation of hydroxyl radicals than the hierarchical CdS/Au/SnO<sub>2</sub>-S heterostructure. Combining the straddle band alignment of SnO<sub>2</sub> and CdS, it can be reasonably postulated that their direct contact in the CdS/Au/SnO<sub>2</sub>-F might give rise to a typical Type-II charge transfer pathway, where a limited portion of photogenerated electrons in CB of CdS can migrate to SnO<sub>2</sub> due to the higher CB potential of CdS. Since the deposited SnO<sub>2</sub> is spatially separated from the conductive substrate, these disoriented electrons in SnO<sub>2</sub> cannot be driven to the counter electrode for hydrogen evolution, thus causing the deteriorated PEC performance. In addition, the partial construction of Type-II heterojunctions is also responsible for the weaker PL signal for the detection of  $\cdot\text{OH}$ . Conceivably, the core-shell CdS/SnO<sub>2</sub> sample without electron mediators will devote more energy to the higher ratio of straddle charge transport. Such behavior ultimately accounts for its lowest photoresponse compared to that in CdS/Au/SnO<sub>2</sub>-F and CdS/Au/SnO<sub>2</sub>-S photoelectrodes. The above analysis also implies the imperfect direct Z-scheme heterojunction built in binary CdS/SnO<sub>2</sub> sample and its

disordered charge transfer.

#### 4. Conclusion

In summary, a novel 1D hierarchical CdS/Au/SnO<sub>2</sub>-S nanostructure has been successfully fabricated and demonstrated as a pure Z-scheme photoanode for highly efficient PEC hydrogen evolution. Compared to the pristine CdS, plasmonic CdS/Au, and direct Z-scheme CdS/SnO<sub>2</sub> heterostructures, the hierarchical CdS/Au/SnO<sub>2</sub>-S photoanode presents the highest photocurrent density and photo-to-current conversion efficiency. This significantly improved PEC performance mainly depends on the effectiveness of strengthened vectorial Z-scheme charge transfer from the CB of SnO<sub>2</sub> to the VB of CdS using Au NPs as charge mediator, which is in favor of the promoted charge separation, increased carrier density, and preserved strong redox capability. More importantly, thanks to the undermined VB holes of CdS and transferred surface oxidation sites, the resulting Z-scheme CdS/Au/SnO<sub>2</sub>-S photoanode exhibits better corrosion resistance and photostability, illustrating its great potential for future applications. In addition, for comparison, a complete SnO<sub>2</sub>-encapsulated CdS/Au (CdS/Au/SnO<sub>2</sub>-F) photoelectrode was also fabricated by full-spectrum irradiation, which exhibits the decreased photo-response and weakened generation of hydroxyl radicals because of the disordered charge transfer. It is thus concluded that the absolute separation of semiconductor components by charge mediators can favor to the construction of pure all-solid-state Z-scheme heterojunctions for better PEC properties. The present work gives a deep



insight into the use of the all-solid-state Z-scheme photoanode for PEC hydrogen generation and provides a valuable strategy to design and fabricate other pure Z-scheme photoelectrodes, which is helpful to push forward the advancement of Z-scheme photosystems for their practical applications.

### CRedit authorship contribution statement

**Zhiyuan Peng:** Conceived and designed the analysis, Collected the data, Contributed data or analysis tools, Contributed data Performed the analysis, Wrote the paper, Other contribution. **Yilu Su:** Conceived the idea, Collected the data, Contributed data or analysis tools Contributed data, Performed the analysis, Wrote the paper, Other contribution, Modification and correction. **Mohamed Siag:** Conceived and supervised the work, Collected the data, Contributed data or analysis tools Contributed data, Performed the analysis, Wrote the paper, Other contribution, Modification and correction.

### Declaration of Competing Interest

The authors declare that they have no known competing financial interests or personal relationships that could have appeared to influence the work reported in this paper.

### Data availability

Data will be made available on request.

### Acknowledgements

We thank the Natural Sciences and Engineering Research Council of Canada (NSERC), the Canada Research Chairs Program (CRC) and Canada Foundation for Innovation (CFI). We thank the China Scholarship Council (CSC Scholarship). NanoQAM center at UQAM is gratefully acknowledged for all the characterization experiments. We thank Quebec Centre for Advanced Materials (QCAM) and Maziar Jafari for helping us to do the ICP-OES measurements during the revision process.

### Appendix A. Supporting information

Supplementary data associated with this article can be found in the online version at [doi:10.1016/j.apcatb.2023.122614](https://doi.org/10.1016/j.apcatb.2023.122614).

### References

- [1] S. Cao, X. Yan, Z. Kang, Q. Liang, X. Liao, Y. Zhang, Band alignment engineering for improved performance and stability of  $\text{ZnFe}_2\text{O}_4$  modified  $\text{CdS}/\text{ZnO}$  nanostructured photoanode for PEC water splitting, *Nano Energy* 24 (2016) 25–31, <https://doi.org/10.1016/j.nanoen.2016.04.001>.
- [2] J. Fu, Z. Fan, M. Nakabayashi, H. Ju, N. Pastukhova, Y. Xiao, C. Feng, N. Shibata, K. Domen, Y. Li, Interface engineering of  $\text{Ta}_3\text{N}_5$  thin film photoanode for highly efficient photoelectrochemical water splitting, *Nat. Commun.* 13 (2022) 729, <https://doi.org/10.1038/s41467-022-28415-4>.
- [3] M.G. Walter, E.L. Warren, J.R. McKone, S.W. Boettcher, Q. Mi, E.A. Santori, N. S. Lewis, Solar water splitting cells, *Chem. Rev.* 110 (2010) 6446–6473, <https://doi.org/10.1021/cr1002326>.
- [4] Y. Li, J.Z. Zhang, Hydrogen generation from photoelectrochemical water splitting based on nanomaterials, *Laser Photonics Rev.* 4 (2010) 517–528, <https://doi.org/10.1002/lpor.200910025>.
- [5] Q. Lu, Y. Yu, Q. Ma, B. Chen, H. Zhang, 2D transition-metal-dichalcogenide-nanosheet-based composites for photocatalytic and electrocatalytic hydrogen evolution reactions, *Adv. Mater.* 28 (2016) 1917–1933, <https://doi.org/10.1002/adma.201503270>.
- [6] T. Hisatomi, J. Kubota, K. Domen, Recent advances in semiconductors for photocatalytic and photoelectrochemical water splitting, *Chem. Soc. Rev.* 43 (2014) 7520–7535, <https://doi.org/10.1039/C3CS60378D>.
- [7] A. Paracchino, V. Laporte, K. Sivula, M. Grätzel, E. Thimsen, Highly active oxide photocathode for photoelectrochemical water reduction, *Nat. Mater.* 10 (2011) 456–461, <https://doi.org/10.1038/nmat3017>.
- [8] D. Shao, Y. Cheng, J. He, D. Feng, L. Zheng, L. Zheng, X. Zhang, J. Xu, W. Wang, W. Wang, A spatially separated organic–inorganic hybrid photoelectrochemical cell for unassisted overall water splitting, *ACS Catal.* 7 (2017) 5308–5315, <https://doi.org/10.1021/acscatal.7b01002>.
- [9] A. Kargar, K. Sun, Y. Jing, C. Choi, H. Jeong, G.Y. Jung, S. Jin, D. Wang, 3D Branched nanowire photoelectrochemical electrodes for efficient solar water splitting, *ACS Nano* 7 (2013) 9407–9415, <https://doi.org/10.1021/nn404170y>.
- [10] T. Wang, Z. Luo, C. Li, J. Gong, Controllable fabrication of nanostructured materials for photoelectrochemical water splitting via atomic layer deposition, *Chem. Soc. Rev.* 43 (2014) 7469–7484, <https://doi.org/10.1039/C3CS60370A>.
- [11] X. Zhang, P. Zhai, Y. Zhang, Y. Wu, C. Wang, L. Ran, J. Gao, Z. Li, B. Zhang, Z. Fan, Engineering single-atomic Ni–N<sub>4</sub>–O sites on semiconductor photoanodes for high-performance photoelectrochemical water splitting, *J. Am. Chem. Soc.* 143 (2021) 20657–20669, <https://doi.org/10.1021/jacs.1c07391>.
- [12] P. Wen, Y. Sun, H. Li, Z. Liang, H. Wu, J. Zhang, H. Zeng, S.M. Geyer, L. Jiang, A highly active three-dimensional Z-scheme  $\text{ZnO}/\text{Au}/\text{g-C}_3\text{N}_4$  photocathode for efficient photoelectrochemical water splitting, *Appl. Catal. B Environ.* 263 (2020), 118180, <https://doi.org/10.1016/j.apcatb.2019.118180>.
- [13] J.H. Baek, B.J. Kim, G.S. Han, S.W. Hwang, D.R. Kim, I.S. Cho, H.S. Jung,  $\text{BiVO}_4/\text{WO}_3/\text{SnO}_2$  double-heterojunction photoanode with enhanced charge separation and visible-transparency for bias-free solar water-splitting with a perovskite solar cell, *ACS Appl. Mater. Interfaces* 9 (2017) 1479–1487, <https://doi.org/10.1021/acsaami.6b12782>.
- [14] Z. Jiao, X. Guan, M. Wang, Q. Wang, B. Xu, Y. Bi, X.S. Zhao, Undamaged depositing large-area  $\text{ZnO}$  quantum dots/RGO films on photoelectrodes for the construction of pure Z-scheme, *Chem. Eng. J.* 356 (2019) 781–790, <https://doi.org/10.1016/j.cej.2018.09.102>.
- [15] H. Li, Y. Zhou, W. Tu, J. Ye, Z. Zou, State-of-the-art progress in diverse heterostructured photocatalysts toward promoting photocatalytic performance, *Adv. Funct. Mater.* 25 (2015) 998–1013, <https://doi.org/10.1002/adfm.201401636>.
- [16] P. Zhou, J. Yu, M. Jaroniec, All-solid-state Z-scheme photocatalytic systems, *Adv. Mater.* 26 (2014) 4920–4935, <https://doi.org/10.1002/adma.201400288>.
- [17] H. Tada, T. Mitsui, T. Kiyonaga, T. Akita, K. Tanaka, All-solid-state Z-scheme in  $\text{CdS-Au-TiO}_2$  three-component nanojunction system, *Nat. Mater.* 5 (2006) 782–786, <https://doi.org/10.1038/nmat1734>.
- [18] J.-M. Li, H.-Y. Cheng, Y.-H. Chiu, Y.-J. Hsu,  $\text{ZnO-Au-SnO}_2$  Z-scheme photoanodes for remarkable photoelectrochemical water splitting, *Nanoscale* 8 (2016) 15720–15729, <https://doi.org/10.1039/C6NR05605A>.
- [19] D. Zheng, C. Pang, X. Wang, The function-led design of Z-scheme photocatalytic systems based on hollow carbon nitride semiconductors, *Chem. Commun.* 51 (2015) 17467–17470, <https://doi.org/10.1039/C5CC07867A>.
- [20] M. Huang, C. Chen, T. Wang, Q. Sui, K. Zhang, B. Li, Cadmium-sulfide/gold/graphitic-carbon-nitride sandwich heterojunction photocatalyst with regulated electron transfer for boosting carbon-dioxide reduction to hydrocarbon, *J. Colloid Interface Sci.* 613 (2022) 575–586, <https://doi.org/10.1016/j.jcis.2022.01.065>.
- [21] X. Wang, S. Li, Y. Ma, H. Yu, J. Yu,  $\text{H}_2\text{WO}_4\cdot\text{H}_2\text{O}/\text{Ag}/\text{AgCl}$  composite nanoplates: a plasmonic S-scheme visible-light photocatalyst, *J. Phys. Chem. C* 115 (2011) 14648–14655, <https://doi.org/10.1021/jp2037476>.
- [22] Z. Chen, F. Bing, Q. Liu, Z. Zhang, X. Fang, Novel Z-scheme visible-light-driven  $\text{Ag}_3\text{PO}_4/\text{Ag}/\text{SiC}$  photocatalysts with enhanced photocatalytic activity, *J. Mater. Chem. A* 3 (2015) 4652–4658, <https://doi.org/10.1039/C4TA06530A>.
- [23] Y. Wang, J. Tang, Z. Peng, Y. Wang, D. Jia, B. Kong, A.A. Elzatahry, D. Zhao, G. Zheng, Fully solar-powered photoelectrochemical conversion for simultaneous energy storage and chemical sensing, *Nano Lett.* 14 (2014) 3668–3673, <https://doi.org/10.1021/nl5014579>.
- [24] Y. Wei, J. Jiao, Z. Zhao, W. Zhong, J. Li, J. Liu, G. Jiang, A. Duan, 3D ordered macroporous  $\text{TiO}_2$ -supported Pt@CdS core-shell nanoparticles: design, synthesis and efficient photocatalytic conversion of  $\text{CO}_2$  with water to methane, *J. Mater. Chem. A* 3 (2015) 11074–11085, <https://doi.org/10.1039/C5TA00444F>.
- [25] Z. Pan, T. Hisatomi, Q. Wang, S. Chen, A. Iwase, M. Nakabayashi, N. Shibata, T. Takata, M. Katayama, T. Minegishi, Photoreduced graphene oxide as a conductive binder to improve the water splitting activity of photocatalyst sheets, *Adv. Funct. Mater.* 26 (2016) 7011–7019, <https://doi.org/10.1002/adfm.201602657>.
- [26] S. Chen, Y. Qi, T. Hisatomi, Q. Ding, T. Asai, Z. Li, S.S.K. Ma, F. Zhang, K. Domen, C. Li, Efficient visible-light-driven Z-scheme overall water splitting using a  $\text{MgTa}_2\text{O}_6\cdot x\text{N}_2/\text{TaON}$  heterostructure photocatalyst for  $\text{H}_2$  evolution, *Angew. Chem.* 127 (2015) 8618–8621, <https://doi.org/10.1002/ange.201502686>.
- [27] Y. Kim, D. Shin, W.J. Chang, H.L. Jang, C.W. Lee, H.E. Lee, K.T. Nam, Hybrid Z-scheme using photosystem I and  $\text{BiVO}_4$  for hydrogen production, *Adv. Funct. Mater.* 25 (2015) 2369–2377, <https://doi.org/10.1002/adfm.201404556>.
- [28] J. Xian, D. Li, J. Chen, X. Li, M. He, Y. Shao, L. Yu, J. Fang,  $\text{TiO}_2$  nanotube array-graphene- $\text{CdS}$  quantum dots composite film in Z-scheme with enhanced photoactivity and photostability, *ACS Appl. Mater. Interfaces* 6 (2014) 13157–13166, <https://doi.org/10.1021/am5029999>.
- [29] A. Iwase, Y.H. Ng, Y. Ishiguro, A. Kudo, R. Amal, Reduced graphene oxide as a solid-state electron mediator in Z-scheme photocatalytic water splitting under visible light, *J. Am. Chem. Soc.* 133 (2011) 11054–11057, <https://doi.org/10.1021/ja203296z>.
- [30] C. Liu, J. Tang, H.M. Chen, B. Liu, P. Yang, A fully integrated nanosystem of semiconductor nanowires for direct solar water splitting, *Nano Lett.* 13 (2013) 2989–2992, <https://doi.org/10.1021/nl401615t>.
- [31] Y.-S. Chen, J.S. Manser, P.V. Kamat, All solution-processed lead halide perovskite- $\text{BiVO}_4$  tandem assembly for photolytic solar fuels production, *J. Am. Chem. Soc.* 137 (2015) 974–981, <https://doi.org/10.1021/ja511739y>.
- [32] W. Wang, H. Wang, Q. Zhu, W. Qin, G. Han, J.R. Shen, X. Zong, C. Li, Spatially separated photosystem II and a silicon photoelectrochemical cell for overall water



- splitting: a natural-artificial photosynthetic hybrid, *Angew. Chem.* 128 (2016) 9375–9379, <https://doi.org/10.1002/ange.201604091>.
- [33] M. Gopannagari, D.P. Kumar, D.A. Reddy, S. Hong, M.I. Song, T.K. Kim, In situ preparation of few-layered WS<sub>2</sub> nanosheets and exfoliation into bilayers on CdS nanorods for ultrafast charge carrier migrations toward enhanced photocatalytic hydrogen production, *J. Catal.* 351 (2017) 153–160, <https://doi.org/10.1021/acscuschemeng.7b00978>.
- [34] Q. Li, B. Guo, J. Yu, J. Ran, B. Zhang, H. Yan, J.R. Gong, Highly efficient visible-light-driven photocatalytic hydrogen production of CdS-cluster-decorated graphene nanosheets, *J. Am. Chem. Soc.* 133 (2011) 10878–10884, <https://doi.org/10.1021/ja2025454>.
- [35] Z. Peng, J. Zhang, P. Liu, J. Claverie, M. Sij, One-dimensional CdS/carbon/Au plasmonic nanorod array photoanodes via in situ reduction-graphitization approach toward efficient solar hydrogen evolution, *ACS Appl. Mater. Interfaces* 13 (2021) 34658–34670, <https://doi.org/10.1021/acsami.1c04006>.
- [36] H. Guan, S. Zhang, X. Cai, Q. Gao, X. Yu, X. Zhou, F. Peng, Y. Fang, S. Yang, CdS@Ni<sub>3</sub>S<sub>2</sub> core-shell nanorod arrays on nickel foam: a multifunctional catalyst for efficient electrochemical catalytic, photoelectrochemical and photocatalytic H<sub>2</sub> production reaction, *J. Mater. Chem. A* 7 (2019) 2560–2574, <https://doi.org/10.1039/C8TA08837C>.
- [37] L. Wang, W. Wang, Y. Chen, L. Yao, X. Zhao, H. Shi, M. Cao, Y. Liang, Heterogeneous p–n junction CdS/Cu<sub>2</sub>O nanorod arrays: synthesis and superior visible-light-driven photoelectrochemical performance for hydrogen evolution, *ACS Appl. Mater. Interfaces* 10 (2018) 11652–11662, <https://doi.org/10.1021/acsami.7b19530>.
- [38] M. Sun, W. Fu, Q. Li, G. Yin, K. Chi, X. Zhou, J. Ma, L. Yang, Y. Mu, Y. Chen, Facile fabrication of CdS nanorod arrays on the transparent conducting substrates and their photoelectrochemical properties, *J. Cryst. Growth* 377 (2013) 112–117, <https://doi.org/10.1016/j.jcrysgro.2013.05.013>.
- [39] Y. Huang, Y. Xu, J. Zhang, X. Yin, Y. Guo, B. Zhang, Hierarchical ultrathin-branched CdS nanowire arrays with enhanced photocatalytic performance, *J. Mater. Chem. A* 3 (2015) 19507–19516, <https://doi.org/10.1039/C5TA05422B>.
- [40] Y. Fu, F. Cao, F. Wu, Z. Diao, J. Chen, S. Shen, L. Li, Phase-modulated band alignment in CdS nanorod/SnS<sub>x</sub> nanosheet hierarchical heterojunctions toward efficient water splitting, *Adv. Funct. Mater.* 28 (2018) 1706785, <https://doi.org/10.1002/adfm.201706785>.
- [41] D. Zhang, L. Liu, L. Zhang, K. Qi, H. Zhang, X. Cui, An anti-photocorrosive photoanode based on a CdS/Ni<sub>3</sub>S<sub>2</sub>@NF heterostructure for visible-light-driven water splitting, *Appl. Surf. Sci.* 420 (2017) 161–166, <https://doi.org/10.1016/j.apsusc.2017.05.144>.
- [42] S. Hong, D.P. Kumar, D.A. Reddy, J. Choi, T.K. Kim, Excellent photocatalytic hydrogen production over CdS nanorods via using noble metal-free copper molybdenum sulfide (Cu<sub>2</sub>MoS<sub>4</sub>) nanosheets as co-catalysts, *Appl. Surf. Sci.* 396 (2017) 421–429, <https://doi.org/10.1016/j.apsusc.2016.10.171>.
- [43] G. Yu, X. Wang, J. Cao, S. Wu, W. Yan, G. Liu, Plasmonic Au nanoparticles embedding enhances the activity and stability of CdS for photocatalytic hydrogen evolution, *Chem. Commun.* 52 (2016) 2394–2397, <https://doi.org/10.1039/C5CC10066F>.
- [44] W. Wang, C. Jin, L. Qi, Hierarchical CdS nanorod@SnO<sub>2</sub> nanobowl arrays for efficient and stable photoelectrochemical hydrogen generation, *Small* 14 (2018) 1801352, <https://doi.org/10.1002/sml.201801352>.
- [45] X. Zhang, Y. Liu, Z. Kang, 3D branched ZnO nanowire arrays decorated with plasmonic Au nanoparticles for high-performance photoelectrochemical water splitting, *ACS Appl. Mater. Interfaces* 6 (2014) 4480–4489, <https://doi.org/10.1021/am500234v>.
- [46] S. Linic, P. Christopher, D.B. Ingram, Plasmonic-metal nanostructures for efficient conversion of solar to chemical energy, *Nat. Mater.* 10 (2011) 911–921, <https://doi.org/10.1038/nmat3151>.
- [47] T. Zhu, Y. Liang, Y. Wang, J. Wang, W. Wang, J. Fu, L. Yao, Y. Cheng, H. Han, P-type β-Ni(OH)<sub>2</sub> nanoparticles sensitize CdS nanorod array photoanode to prolong charge carrier lifetime and highly improve bias-free visible-light-driven H<sub>2</sub> evaluation, *Appl. Catal. B Environ.* 271 (2020), 118945, <https://doi.org/10.1016/j.apcatb.2020.118945>.
- [48] L. Yao, W. Wang, T. Zhu, Y. Wang, Y. Liang, J. Fu, J. Wang, Y. Cheng, S. Liu, A rational design of CdS/ZnFe<sub>2</sub>O<sub>4</sub>/Cu<sub>2</sub>O core-shell nanorod array photoanode with stair-like type-II band alignment for highly efficient bias-free visible-light-driven H<sub>2</sub> generation, *Appl. Catal. B Environ.* 268 (2020), 118460, <https://doi.org/10.1016/j.apcatb.2019.118460>.
- [49] T.A. Ho, C. Bae, J. Joe, H. Yang, S. Kim, J.H. Park, H. Shin, Heterojunction photoanode of atomic-layer-deposited MoS<sub>2</sub> on single-crystalline CdS nanorod arrays, *ACS Appl. Mater. Interfaces* 11 (2019) 37586–37594, <https://doi.org/10.1021/acsami.9b11178>.
- [50] L. Qin, D. Huang, P. Xu, G. Zeng, C. Lai, Y. Fu, H. Yi, B. Li, C. Zhang, M. Cheng, C. Zhou, X. Wen, In-situ deposition of gold nanoparticles onto polydopamine-decorated g-C<sub>3</sub>N<sub>4</sub> for highly efficient reduction of nitroaromatics in environmental water purification, *J. Colloid Interface Sci.* 534 (2019) 357–369, <https://doi.org/10.1016/j.jcis.2018.09.051>.
- [51] C. Lin, J. Fu, S. Liu, Facile preparation of Au nanoparticle-embedded polydopamine hollow microcapsule and its catalytic activity for the reduction of methylene blue, *J. Macromol. Sci. A* 56 (2019) 1104–1113, <https://doi.org/10.1080/10601325.2019.1658526>.
- [52] M. Huang, T. Wang, Z. Wu, Y. Shang, Y. Zhao, B. Li, Rational fabrication of cadmium-sulfide/graphitic-carbon-nitride/hematite photocatalyst with type II and Z-scheme tandem heterojunctions to promote photocatalytic carbon dioxide reduction, *J. Colloid Interface Sci.* 628 (2022) 129–140, <https://doi.org/10.1016/j.jcis.2022.08.059>.
- [53] Z. Zheng, F. Han, B. Xing, X. Han, B. Li, Synthesis of Fe<sub>3</sub>O<sub>4</sub>@CdS@CQDs ternary core-shell heterostructures as a magnetically recoverable photocatalyst for selective alcohol oxidation coupled with H<sub>2</sub>O<sub>2</sub> production, *J. Colloid Interface Sci.* 624 (2022) 460–470, <https://doi.org/10.1016/j.jcis.2022.05.161>.
- [54] X. Long, L. Gao, F. Li, Y. Hu, S. Wei, C. Wang, T. Wang, J. Jin, J. Ma, Bamboo shoots shaped FeVO<sub>4</sub> passivated ZnO nanorods photoanode for improved charge separation/transfer process towards efficient solar water splitting, *Appl. Catal. B Environ.* 257 (2019), 117813, <https://doi.org/10.1016/j.apcatb.2019.117813>.
- [55] J. Mu, F. Teng, H. Miao, Y. Wang, X. Hu, In-situ oxidation fabrication of 0D/2D SnO<sub>2</sub>/SnS<sub>2</sub> novel Step-scheme heterojunctions with enhanced photoelectrochemical activity for water splitting, *Appl. Surf. Sci.* 501 (2020), 143974, <https://doi.org/10.1016/j.apsusc.2019.143974>.
- [56] Z. Zhang, M. Choi, M. Baek, Z. Deng, K. Yong, Plasmonic and passivation effects of Au decorated RGO/CdSe nanofilm uplited by CdSe@ZnO nanorods with photoelectrochemical enhancement, *Nano Energy* 21 (2016) 185–197, <https://doi.org/10.1016/j.nanoen.2016.01.020>.
- [57] J. Yu, J. Jin, B. Cheng, M. Jaroniec, A noble metal-free reduced graphene oxide-CdS nanorod composite for the enhanced visible-light photocatalytic reduction of CO<sub>2</sub> to solar fuel, *J. Mater. Chem. A* 2 (2014) 3407–3416, <https://doi.org/10.1039/C3TA14493C>.
- [58] K.-H. Cho, Y.-M. Sung, The formation of Z-scheme CdS/CdO nanorods on FTO substrates: the shell thickness effects on the flat band potentials, *Nano Energy* 36 (2017) 176–185, <https://doi.org/10.1016/j.nanoen.2017.04.037>.
- [59] X. Zhu, N. Gujjarro, Y. Liu, P. Schouwink, R.A. Wells, F. Le Formal, S. Sun, C. Gao, K. Sivula, Spinel structural disorder influences solar-water-splitting performance of ZnFe<sub>2</sub>O<sub>4</sub> nanorod photoanodes, *Adv. Mater.* 30 (2018) 1801612, <https://doi.org/10.1002/adma.201801612>.
- [60] B. Baral, K. Parida, {040/110} facet isotype heterojunctions with monoclinic scheelite BiVO<sub>4</sub>, *Inorg. Chem.* 59 (2020) 10328–10342, <https://doi.org/10.1021/acs.inorgchem.0c01465>.
- [61] H. Xu, W. Fan, Y. Zhao, B. Chen, Y. Gao, X. Chen, D. Xu, W. Shi, Amorphous iron (III)-borate decorated electrochemically treated-BiVO<sub>4</sub> photoanode for efficient photoelectrochemical water splitting, *Chem. Eng. J.* 411 (2021), 128480, <https://doi.org/10.1016/j.cej.2021.128480>.
- [62] B. Zhang, X. Huang, Y. Zhang, G. Lu, L. Chou, Y. Bi, Unveiling the activity and stability origin of BiVO<sub>4</sub> photoanodes with FeNi oxyhydroxides for oxygen evolution, *Angew. Chem. Int. Ed.* 59 (2020) 18990–18995, <https://doi.org/10.1002/anie.202008198>.
- [63] J.S. DuChene, B.C. Sweeny, A.C. Johnston-Peck, D. Su, E.A. Stach, W.D. Wei, Prolonged hot electron dynamics in plasmonic-metal/semiconductor heterostructures with implications for solar photocatalysis, *Angew. Chem. Int. Ed.* 53 (2014) 7887–7891, <https://doi.org/10.1002/anie.201404259>.
- [64] M. Zhong, T. Hisatomi, Y. Kuang, J. Zhao, M. Liu, A. Iwase, Q. Jia, H. Nishiyama, T. Minegishi, M. Nakabayashi, Surface modification of CoO<sub>x</sub> loaded BiVO<sub>4</sub> photoanodes with ultrathin p-type NiO layers for improved solar water oxidation, *J. Am. Chem. Soc.* 137 (2015) 5053–5060, <https://doi.org/10.1021/jacs.5b00256>.
- [65] Y. Chen, L. Wang, R. Gao, Y.-C. Zhang, L. Pan, C. Huang, K. Liu, X.-Y. Chang, X. Zhang, J.-J. Zou, Polarization-enhanced direct Z-scheme ZnO-WO<sub>3-x</sub> nanorod arrays for efficient piezoelectric-photoelectrochemical water splitting, *Appl. Catal. B Environ.* 259 (2019), 118079, <https://doi.org/10.1016/j.apcatb.2019.118079>.
- [66] L. Ran, S. Qiu, P. Zhai, Z. Li, J. Gao, X. Zhang, B. Zhang, C. Wang, L. Sun, J. Hou, Conformal macroporous inverse opal oxynitride-based photoanode for robust photoelectrochemical water splitting, *J. Am. Chem. Soc.* 143 (2021) 7402–7413, <https://doi.org/10.1021/jacs.1c00946>.
- [67] Y. Song, X. Zhang, Y. Zhang, P. Zhai, Z. Li, D. Jin, J. Cao, C. Wang, B. Zhang, J. Gao, Engineering MoO<sub>x</sub>/MXene hole transfer layers for unexpected boosting of photoelectrochemical water oxidation, *Angew. Chem.* 134 (2022), e202200946, <https://doi.org/10.1002/ange.202200946>.